Cooperative Jahn-Teller phase transition in $PrAlO_3$

R. J. Birgeneau
Bell Laboratories, Murray Hill, New Jersey 07974
*and Brookhaven National Laboratory, Upton, New York 11973**

J. K. Kjems† and G. Shirane
*Brookhaven National Laboratory, Upton, New York 11973**

L. G. Van Uitert
Bell Laboratories, Murray Hill, New Jersey 07974
(Received 30 April 1974)

The perovskite $PrAlO_3$ is known to exhibit an apparently complicated series of structural phase transitions from cubic to rhombohedral to orthorhombic to monoclinic and ultimately tetragonal symmetry at temperatures of 1320, 205, and 151 K, respectively. The 1320-K cubic-rhombohedral transition is a simple soft R_{25} phonon transition as observed in $LaAlO_3$ and $SrTiO_3$. In $PrAlO_3$ it results in a crystal structure in which the AlO_6 octahedra are rotated by about 9° in a staggered sense about the [111] axis. Harley *et al.* have suggested that the first-order 205-K and second-order 151-K transitions occur as a result of a delicate interplay between the anharmonic lattice interactions which prefer a rhombohedral structure and the R_{25} phonon-Pr^{3+} ($4f^2$) coupling which prefers an orthorhombic and ultimately a tetragonal structure. In this paper we report an extensive elastic and inelastic neutron scattering study of $PrAlO_3$ with special emphasis on the 151-K transition. We also have carried out a detailed crystal-field analysis of the Pr^{3+} energy levels in all phases. Our crystallographic measurements of the lattice constants and angles as a function of temperature are consistent with a structural model in which the over-all AlO_6 rotation angle is constant in magnitude, but the rotation axis itself moves continuously from [101] to [001] as the temperature is lowered from 151 to ~70 K. Neutron scattering measurements of the crystal-field levels are reported and by combining these with previous results a full crystal-field level scheme is constructed for the Pr^{3+} ion. The temperature dependence of the crystal-field splittings is then semiquantitatively predicted via a simple model with fixed fourth- and sixth-order terms and a constant electric-field gradient tensor in which the principal axis rotates in unison with the AlO_6 axis from [101] to [001]. With the above as a basis, it is shown that the 151-K transition corresponds to a simple cooperative Jahn-Teller transition involving a single electronic mode (in this case a quadrupole exciton), a $B_1(C_{2v})$ optical phonon, and a $B_1(C_{2v})$ acoustic mode, the perovskite Σ_3 $[101]_{T2}$ phonon. Accurate measurements of the acoustic-phonon order parameter are reported; it is found that the strain follows the mean-field power law $e_{zz}-e_{xx} \sim (1-T/T_c)^{0.50\pm0.02}$ for $10^{-1} < 1-T/T_c < 10^{-3}$. In addition, the normalized order parameter is shown to coincide at all temperatures with independently measured electronic and condensed-optical-phonon order parameters. The coupled exciton-acoustic-phonon dispersion relations have been measured through T_c and analyzed using the theory of Elliott *et al*. The principal results are the following: (a) The $[101]_{T2}$ phonon is the soft mode of the system. (b) The quadrupole exciton is observed directly over a wide range of k in the region where it anticrosses the phonon. (c) An analysis of the coupled dispersion relations at T_c yields separately the k-dependent phonon-induced Pr^{3+} quadrupole-quadrupole interactions arising from the coupling to the B_1 acoustic and optic modes; the former is found to account for about 1/3 of the total interaction at $k=0$ and to have a mean range of 30 Å. (d) The theory of Elliott *et al.* is found to predict quantitatively the temperature dependence of the soft-acoustic-phonon dispersion relation above T_c. This work thence established the 151-K transition in $PrA1O_3$ as a prototype coupled pseudospin-phonon structural phase transition.

I. INTRODUCTION

In the past decade there has been a concerted experimental and theoretical effort on the problem of structural phase transitions in solids.[1] Structural phase transitions have traditionally been classified into two broad groups: (a) *the displacive type*, the displacement of atoms are described by spatially continuous variables; (b) *the order-disorder type*, the possible positions of atoms involved in the transition are spatially discrete rather than continuous; the variable which plays the role of the order parameter is then described by a pseudospin variable. As discussed most recently by Yamada *et al.*,[2] however, there is a third group of transitions: (c) *the pseudospin-phonon coupled case*. This represents a convolution of types (a) and (b) in which there is a strong coupling between the order-disorder and displacive variables in the crystal and most importantly in which the phase

transition itself may be driven by this coupling. Examples of type (c) include ferroelectric phase transitions triggered by the ordering of the protons as in potassium dihydrogen phosphate (KDP),[3] order-disorder transitions in crystals such as ND_4^- Br where the orientational order of the molecular groups takes place accompanied by the condensation of phonon modes,[2] and cooperative Jahn-Teller transitions[4] where the ordering occurs in the electronic degrees of freedom and the transition is driven by the electron-phonon coupling.

The cooperative Jahn-Teller effect (CJTE) has been the subject of intense theoretical and experimental research for the past few years.[4-7] This interest has been stimulated especially by the discovery of rather clean examples of the CJTE in certain rare-earth vanadate and arsenate crystals.[4,8-10] The theory for the CJTE in rare-earth insulators turns out to have a number of simplifying features mainly because of the hierarchy of intra-atomic and interatomic interactions determining the rare-earth 4f-electron energy levels. In the ideal situation one has as the ground state a simple orbital doublet which is either degenerate or nearly degenerate and which couples to the lattice through the electric field gradient created at the rare-earth site by the phonon displacements. This gives rise to an effective electric quadrupole-quadrupole interaction (EQQI) mediated by the phonons.[11] In the simplest case where phonons of one particular symmetry dominate, the CJTE becomes isomorphous to the $S=\frac{1}{2}$ Ising model in a transverse field. This model Hamiltonian, in turn, has been the subject of extensive study so that a great deal of theoretical information is available.[12-16] For the CJTE a potpourri of interesting effects both in the electronic and lattice dynamical properties have been predicted[4,9] and some of these, particularly $k=0$ phenomena, have been observed experimentally in the vanadates.[4,9,10] However, for the CJTE in general there have to-date been no studies of the coupled dispersion relations at finite wave vectors nor have there been accurate studies of the critical behavior of the order parameters[7] near T_c.

In this paper we report an extensive experimental investigation of the 151-K structural phase transition in the rare-earth perovskite $PrAlO_3$ using elastic and inelastic neutron scattering techniques. $PrAlO_3$ exhibits an apparently complicated series of structural phase transitions from cubic to rhombohedral to orthorhombic to monoclinic and ultimately to tetragonal symmetry at 1320, 205, and 151 K, respectively.[17-23] The transitions are, respectively, second, first, and second order. The 1320-K cubic-rhombohedral transition occurs as a result of an R-point Γ_{25} (hereafter denoted as R_{25}) phonon instability[23,24] as studied extensively previously in $SrTiO_3$ (Refs. 1, 25, and 26) and $LaAlO_3$.[27] In a recent paper, Harley *et al.*[20] have suggested that the 205 and 151-K transitions occur as a result of a competition between the anharmonic lattice interactions which stabilize the rhombohedral phase and the R_{25}-phonon–Pr^{3+}-4f-electron interaction which favors an orthorhombic and ultimately a tetragonal structure. Our results confirm the basic hypothesis of their model although there are a number of quantitative disagreements. Most importantly we find that the 151-K transition, in fact, represents a rather simple example of the CJTE. It involves a singly degenerate electronic mode linearly coupled to an acoustic- and an optical-phonon mode of the same symmetry.

We have carried out detailed measurements of the coupled acoustic-phonon-exciton dispersion relations through $T_c=151$ K, and we have analyzed these using the random-phase approximation (RPA) theory of Elliott *et al.* The soft mode of the transition is found to be the $[101]_{T_2}$ acoustic mode as expected on the basis of symmetry. An analysis of the coupled dispersion relations at T_c yields directly the components of the wave-vector-dependent EQQI originating from both the acoustic- and the optic-phonon-mode coupling. We have also measured with high resolution the strain $e_{zz}-e_{xx}$ which functions as the acoustic-phonon order parameter[4,7] of the Jahn-Teller transition. The electronic order parameter may be extracted from existing fluorescence data while the condensed-optical-phonon order parameter has been determined via EPR by Cohen *et al.*[22] Thus an intercomparison of the three principal order parameters in the CJTE is possible.

In addition to the above detailed study of the 151-K transition, we have also carried out a more general survey of the crystallographic and crystal-field properties of $PrAlO_3$ over a wide range of temperatures. Gratifyingly we find that with rather simple assumptions based on the Harley *et al.*[20] hypothesis one can account semiquantitatively for the behavior of the crystal-field levels over a wide range of temperatures. An interesting feature of $PrAlO_3$ is that in order to arrive at a satisfactory picture it is necessary to combine neutron and x-ray[19] crystallographic measurements, Raman scattering and fluorescence,[20] inelastic neutron scattering, impurity EPR[22] and specific-heat results.[28] As we shall show, most of these diverse experimental results can be satisfactorily understood although a few puzzles, particularly in the optical studies, do remain.

The format of this paper is as follows. In Sec. II we give a variety of preliminary details including a discussion of the crystallographic, etc., data

available before this study, the basic model of Harley *et al.*,[20] and the neutron scattering experimental techniques. Section III contains a discussion of our crystallographic measurements and neutron crystal-field spectroscopy together with a detailed crystal-field analysis of the Pr^{3+} ($4f^2$) energy levels as a function of temperature. Section IV discusses the 151-K transition as a cooperative Jahn-Teller transition. Here the measurement and analysis of the coupled exciton-phonon modes are presented together with a discussion of the associated order parameters. Finally, Sec. V contains suggestions for further experiments and theory.

As an aside, we should perhaps note that this article reports the results of an extended, detailed study of $PrAlO_3$. We have decided to publish essentially all of the information so-obtained in this single comprehensive paper. Two brief notes, one on the exciton-phonon dynamics above 151 K (Ref. 21) and a second on the order parameters[22] below 151 K in $PrAlO_3$ have been published recently; the reader is referred to these papers for a cursory summary. The reader who is interested primarily in the crystallography and crystal-field effects in $PrAlO_3$ need only read Sec. III while the reader primarily interested in the CJTE need only peruse the figures and read Sec. IV.

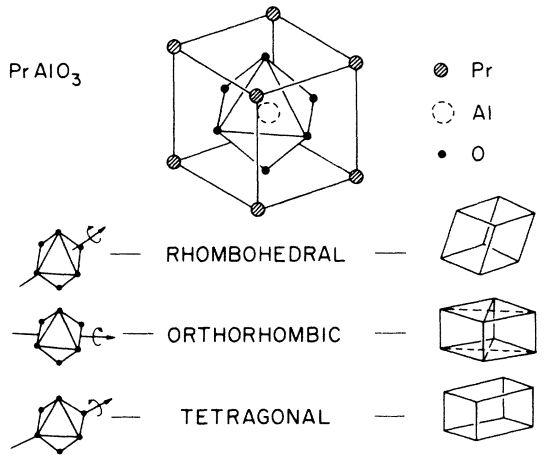

FIG. 1. Cubic perovskite structure shown as a CsCl arrangement of Pr atoms and AlO_6 octahedra. The relations between various rotations of the octahedra and the distortions of the unit cell are shown schematically.

II. PRELIMINARY DETAILS

A. General characteristics of $PrAlO_3$

As discussed in the Introduction, $PrAlO_3$ crystallizes in the perovskite structure as illustrated in Fig. 1. At ~1320 K the crystal undergoes a structural phase transition from cubic to a rhombohedral symmetry. An x-ray study by Burbank[19] has shown that at room temperature the rhombohedral structure may be generated from the cubic structure by rotating the AlO_6 octahedra alternately by ~±8° about the [111] axis. Concomitantly, the crystal compresses by about 1% along the [111] axis and the cell angles differ from 90° by an amount $\delta = 0.35°$. This structure is essentially identical to that of the isomorphic crystal $LaAlO_3$ (Ref. 27) which undergoes a cubic-rhombohedral phase transition at ~800 K. The space group is D_{3d}^6 and the point symmetry at the rare-earth site is D_{3d}. This phase transition is driven by an instability in the R_{25} phonon in the cubic phase. The R_{25} phonon is a triply degenerate mode whose eigenvectors correspond to staggered rotations of the AlO_6 octahedra about the perovskite axes. This type of phase transition has been thoroughly explored in the context of both $SrTiO_3$ and $LaAlO_3$.[1]

Before continuing with a discussion of the crystallography, we consider briefly a simplified theory for such a phase transition. Following Slonczewski and Thomas,[29] the elastic energy for a perovskite crystal, including both the strain and AlO_6 rotation contributions, may be written

$$U = \tfrac{1}{2}\, a\vec{Q}^2 + \tfrac{1}{4}\, b\,(Q_x^4 + Q_y^4 + Q_z^4) + \tfrac{1}{2}\, c\,(Q_x^2Q_y^2 + Q_y^2Q_z^2 + Q_z^2Q_x^2)$$
$$- B_e[(2e_{xx} - e_{yy} - e_{zz})Q_x^2 + (2e_{yy} - e_{zz} - e_{xx})Q_y^2 + (2e_{zz} - e_{xx} - e_{yy})Q_z^2] - B_t(e_{yz}Q_yQ_z + e_{zx}Q_zQ_x + e_{xy}Q_xQ_y)$$
$$+ \tfrac{1}{2}\, C_{11}(e_{xx}^2 + e_{yy}^2 + e_{zz}^2) + C_{12}(e_{xx}e_{yy} + e_{yy}e_{zz} + e_{zz}e_{xx}) + \tfrac{1}{2}\, C_{44}(e_{yz}^2 + e_{zx}^2 + e_{xy}^2), \qquad (1)$$

where $\vec{Q}$ is the rotation vector for the staggered rotation of the AlO_6 octahedra defined such that the actual displacement of the ith oxygen atom in the lth cell is given by

$$u_{il} = (-)^l \vec{r}_i \times \vec{Q}\,. \qquad (2)$$

The conventional definition[30] of the microscopic strains are used for the $e_{\alpha\beta}$ and for the force constants C_{ij}.

In the simplest theory the R_{25} phase transition occurs when a changes sign.[31] In the transformed phase then the absolute minimum of U occurs for $\vec{Q} = (Q, 0, 0)$ or $(1/\sqrt{3})(Q, Q, Q)$ depending on the relative magnitude of the coefficients b, c, etc.[29,31]

If one ignores the strain contribution, then one finds that the rhombohedral phase is stable if $c > b$; both phases require $b > 0$, $b + 2c > 0$. The energy of the orthorhombic phase is always intermediate between that of the tetragonal and rhombohedral phases, but all three phases have equal energy if $b = c$. As discussed by Slonczewski and Thomas,[29] explicit inclusion of the strains gives one modified b, c's but the instability of the orthorhombic phase remains.

Harley *et al.*[20] have analyzed the room-temperature lattice-dynamical properties of $PrAlO_3$ based on Eq. (1) excluding the strain contributions and ignoring any possible effects from the Pr^{3+} ions. Following Thomas and Müller,[31] the constants a, b, c may be simply deduced from the over-all AlO_6 rotation angle together with the $k = 0$ energies of the low-frequency "soft" phonon modes which arise from the R_{25} phonons of the cubic phase. The values so obtained are listed in Table I. The most important feature of these results is that one finds $c = 0.89b$. Thus the rhombohedral phase is only slightly favored by the anharmonic lattice interactions over the orthorhombic and tetragonal phases. We note that similar results are obtained in $LaAlO_3$. Indeed in a more extensive analysis using self-consistent-phonon theory, Feder and Pytte[32] conclude that in $LaAlO_3$ it is only the strain contribution which stabilizes the rhombohedral phase. In $LaAlO_3$ as the temperature is lowered towards 0 K, the crystal retains its rhombohedral symmetry, and the over-all rotation angle and phonon energies saturate.[1,27] Below room temperature the constants a, b, c, etc., may be taken as essentially temperature independent. Similar results are obtained in $NdAlO_3$.[23]

$PrAlO_3$, on the other hand, exhibits markedly different behavior. As first discovered by Cohen *et al.*,[17] at ~205-K $PrAlO_3$ undergoes a dramatic first-order transition to a pseudo-orthorhombic phase. This transition is followed at 151 K by a second-order transition to a monoclinic structure. From their fluorescence study, however, Cohen *et al.*[17] note that by 80 K the crystal seems to have obtained a tetragonal symmetry with the tetragonal axis coinciding with one of the original perovskite axes. Both the 205- and 151-K transitions are accompanied by marked changes in the Pr^{3+} crystal-field level energies.[17,20] Furthermore, the fluorescence lines are anomalously broad indicating unusually large ion-ion interactions. Specific-heat measurements by Ryder[28] confirm that the 205-K transition is first order and they show a classical second-order specific-heat anomaly at 151 K.

TABLE I. Elastic constants and elastic potential parameters of Eq. (1) in $PrAlO_3$. Elastic potential parameters in units of 10^{12} erg/cm^3.

$a = -0.42$ [a]	$C_{11} - C_{12} = 1.95$ [b]
$b = 24.9$ [a]	$C_{44} = 1.35$ [b]
$c = 22.2$ [a]	$B_e = 0.16$ (160 K)
$B_t = -0.39$	$B_e = 0.32$ (4 K)

[a] Derived by Harley *et al.* (Ref. 20).

[b] Derived from acoustic-phonon dispersion curves at 295 K.

In addition to the x-ray results at 273 K discussed above, Burbank[19] also has carried out a semiquantitative study at 172 and 135 K. At 172 K he finds that the crystal is essentially orthorhombic. The AlO_6 octahedra are rotated about a [101] axis by about 6° and the a, c perovskite axes are expanded slightly relative to the b axis. There is also an indication that the Pr^{3+} ion moves off-center slightly. As a note of caution, however, we should emphasize that Burbank's value of 6° for the rotation angle is only meant to be semiquantitative and that the actual evidence for the Pr^{3+} displacement is a single weak reflection which, in the absence of such a displacement, would have a vanishing intensity. At 135 K the x-ray study indicates that the crystal has suffered a shear of the form $e_{zz} - e_{xx}$ relative to the perovskite axes. From the intensities it is concluded that the octahedra are still rotated about the [101] axis. As we shall discuss later, the EPR experiments[22] are in explicit disagreement with the latter results. However, again the Burbank study was only meant to be qualitative and Burbank did not test for models with octahedra rotated about odd axes in the crystal. No x-ray studies have been performed at 80 K as a check on the apparent tetragonal symmetry indicated by the fluorescence and Raman scattering data.

In the original work of Cohen *et al.*,[17] it is emphasized that the feature which distinguishes $PrAlO_3$ from its isomorphs $LaAlO_3$ and $NdAlO_3$ is the fact that Pr^{3+} is a non-Kramers ion with the configuration $4f^2$. This suggests the possibility of large electric multipole interactions,[33] particularly those mediated by the lattice.[11] In a germane paper Harley *et al.*[20] demonstrate that $PrAlO_3$ is, in fact, much simpler than it would appear superficially; in particular, they propose a straightforward microscopic model following the Cohen *et al.* suggestion which, as we shall see, contains the essential physics of this material.

B. Harley *et al.* model

In the above-mentioned paper, Harley *et al.*[20] present EPR, Raman scattering, and fluorescence studies of $PrAlO_3$. These data, together with those

discussed above, have led them to a theoretical model which seems to account for the principal features of $PrAlO_3$. The EPR experiments on Gd^{3+} substituted for Pr^{3+} show that at 80 K the symmetry at the Pr^{3+} site is tetragonal. From the fluorescence and the Raman scattering experiments, Harley *et al.* determine the energies of most of the Pr^{3+} crystal-field levels as a function of temperature from 4.2 to 180 K. At 4.2 K they are also able to infer the symmetries and degeneracies of the levels. We shall discuss these results in detail in Sec. III. The principal result of Harley *et al.*, however, is that the Pr^{3+} $(4f^2)$-$^3H_4$ lowest manifold is split in the following manner. In the cubic phase the $E_g(O_h)$ orbital doublet is lowest and the first excited state is the T_{2g} triplet at about 250 cm^{-1}. In the rhombohedral phase the lowest doublet remains degenerate while the T_{2g} triplet is split into a singlet and a doublet. In the orthorhombic phase, $151 < T < 205$ K, the cubic E_g doublet is split by 56 cm^{-1}, and the degeneracy of the T_{2g} triplet is completely removed. Finally at 80 K the original cubic E_g doublet levels are separated by 222 cm^{-1}.

These results then lead Harley *et al.* to the following basic hypothesis: *The successive phase transitions in $PrAlO_3$ occur as a result of a competition between the anharmonic lattice interactions which prefer a rhombohedral structure and the electron-phonon coupling of the Pr^{3+} 4f crystal-field levels to the R_{25} phonons which prefers an orthorhombic and ultimately a tetragonal structure.* Thus at high temperatures when all of the crystal-field levels are equally populated, the electronic energies do not play a role and hence purely lattice dynamical considerations determine the crystal structure. However, when the temperature is lowered sufficiently that only the ground doublet and the first excited state are appreciably populated, the crystal can lower its total free energy—electronic plus lattice—by transforming to a structure in which the octahedra are rotated about a [101] axis. That is, the cost in lattice energy is offset by the gain in electronic energy. The fact that $b \simeq c$ in Eq. (1) implies that the cost in lattice energy is in fact rather small. Finally, at lower temperatures the crystal transforms continuously from orthorhombic to tetragonal symmetry in order to effect the largest possible splitting in the ground doublet. In the Harley *et al.* model then the 151-K phase transition involves the AlO_6 rotation axis itself moving continuously from a [101] to an [001] direction. From their optical studies, Harley *et al.* conclude that this process is complete at about 100 K.

An essential feature of the above model is that there is no linear coupling between the Pr^{3+} ion and the R_{25} phonons since the latter transform like T_{2u} at the Pr^{3+} site.[34] Thus when expressed in terms of cubic-crystal eigenfunctions the electron-phonon Hamiltonian contains terms such as $\tilde{O}_{E_g}(Q_z^2 - Q_x^2)$. As noted by Harley *et al.* from the vantage point of the cubic structure, the transition in $PrAlO_3$ are not of the Jahn-Teller type since the latter is strictly linear in the displacement coordinates.[35] However, this distinction is in fact just a matter of semantics. As we shall see, the 151-K transition is driven by the electron-phonon coupling which is indeed linear in the displacement coordinates of the *orthorhombic* phase.

Harley *et al.* have carried out explicit calculations using a simplified version of the above model. The calculation involves writing for the free energy

$$F = U - kT \ln Z , \tag{3}$$

where

$$Z = \sum_{j=1}^{9} e^{-E_j/kT} . \tag{4}$$

U is given by Eq. (1) and the E_j's are the energies of the Pr^{3+} $^3H_4$ energy levels. The latter in turn depend on the Q_α. The equilibrium configuration is then obtained by minimizing F with respect to the Q_α as a function of temperature. Using a model which includes only the E_g and T_{2g} electronic levels and also only E_g-type phonon coupling, Harley *et al.* have shown that it is possible to generate the successive phases actually observed in $PrAlO_3$ with an appropriate choice of parameters. Although their model yields a number of incorrect predictions, it appears their basic hypothesis, at least, does contain the correct physics.

We now proceed to discuss our own experiments and analysis on $PrAlO_3$.

C. Experimental details

The experiments to be described were carried out at the Brookhaven High Flux Beam Reactor using both double-axis and triple-axis constant-Q spectrometry. The bulk of the measurements were performed on a very good quality single-crystal sample with dimensions $2 \times 2 \times 1$ cm. It was grown from a $PbO \cdot PbF_2 \cdot P_2O_3$ flux by slow cooling from 1300 to 950 °C at a rate of 0.5 °/h. This particular sample was transparent with a dark red color probably due to a slight oxygen excess; however, the transition temperatures coincided with those reported for other samples. The crystal was essentially single domain at room temperature and the first-order transition at 205 K was single domain to single domain with appreciable hyster-

esis (~10 K). The 151-K transition resulted in several twinned crystallites which, on the one hand, presented a very suitable tool for measurements of the spontaneous strain but, on the other hand, caused considerable width of the mosaic distributions. However, an apparent single-domain sample with narrow mosiac width was always regained at room temperature. For some measurements a single-domain sample was obtained below 151 K by the application of a magnetic field[18]; approximately 20 kG was sufficient for the present sample at 80 K. The sample for powder diffraction was prepared by finely crushing and sieving material from another batch of small flux-grown crystals.

A typical collimation was 20′ throughout the spectrometer; for each part of the inelastic scattering experiments care was taken to optimize the choice of incident energy. In some cases the criteria was the achievement of optimum triple axis focusing and in others it was optimum energy resolution but the choice was always subject to the demand that higher-order contamination in the incident beam could be effectively removed by the use of pyrolytic graphite filters.[36] Typical incident energies were 8.4, 13.5, and 41 meV with a vertically focusing (002) pyrolytic graphite monochromator and (111) Ge or (002) graphite as analyzers. Typical energy resolutions (full width at half-maximum) were 0.18, 0.40, and 2.2 meV, respectively, at the quoted energies. The powder diffraction was done with a wavelength of 2.46 Å.

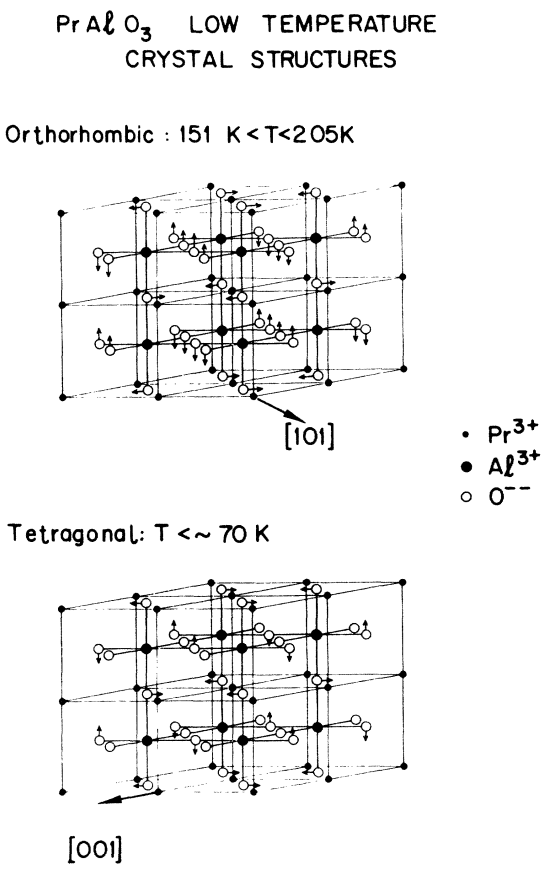

FIG. 2. Diagram of the enlarged unit cells of $PrAlO_3$ in the orthorhombic and tetragonal phases. The over-all rotation of the AlO_6 octahedra is 9.4 ± 0.4 deg in both phases.

III. CRYSTALLOGRAPHY AND CRYSTAL FIELDS

A. Crystallographic measurements

We have already discussed the basic crystallography extensively in Sec. II. The ideal perovskite structure which $PrAlO_3$ possesses above 1320 K is illustrated in Fig. 1. Since all of the crystallographic phases of $PrAlO_3$ represent relatively small distortions from the cubic structure, it is simplest to maintain the perovskite cell as reference for the different measurements. Neutron crystallographic experiments were carried out both with the large single crystal and with the powder. These two techniques are complementary since the former enables one to measure rapidly the lattice constants and angles whereas the latter, being extinction free, is suitable for determining positional parameters.

We consider first the powder measurements. All phases exhibit only those reflections expected on the basis of the R_{25} phonon condensation with two perovskite units per primitive cell. Accurate intensity measurements were carried out for the first eight reflections which include six perovskite and two superlattice peaks. At 220, 165, 77 K the powder spectra are consistent with the suggested rhombohedral, orthorhombic, and tetragonal structures. The latter two structures are illustrated in Fig. 2. In these three phases in terms of perovskite axes, one has, respectively, $a = b = c$, $a = c \neq b$, and $a = b \neq c$. Only in the tetragonal phase could the $(00l)$ and $(h00)$, $(0k0)$ peaks be clearly resolved. The lattice constants deduced from the powder patterns are shown in Fig. 3. The intensities were fitted to a structural model with the Pr^{3+} and Al^{3+} atoms at their perovskite positions and the AlO_6 units rotated by an angle Q about the [111], [101], and [001] axes, respectively. This simple model gives an excellent fit to all intensities with an R factor of ~0.02. The deduced AlO_6 rotation angles are $(8.7 \pm 0.4)°$, $(9.4 \pm 0.4)°$, and $(9.4 \pm 0.4)°$. Thus the over-all rotation angle is nearly temperature independent in spite of the drastic changes in the rotation axis itself. Our

values for the rotation angle are slightly larger than those inferred by Burbank[19]; we believe that this discrepancy originates in the qualitative nature of Burbank's study. We should note also that the powder peak intensities are totally insensitive to small displacements of the Pr^{3+} ions of the sort suggested by Burbank. In any case, none of the principal physical features of $PrAlO_3$ are affected by such displacements so that in the remainder of this paper we shall assume that the Pr^{3+} ions remain in their high-symmetry perovskite positions at all temperatures. The consequent space groups in the three limiting phases are then D_{3d}^6, D_{2h}^{28}, and D_{4h}^{18} with point symmetries at the Pr^{3+} site of D_3, C_{2v}, and D_{2d}.

We now consider the single-crystal measurements. At room temperature the structure is rhombohedral with the lattice constants shown in Fig. 3. The angle between the rhombohedral axes is $(90.25 \pm 0.02)°$. As noted previously, between 151 and 205 K the crystal is orthorhombic with $a = c \neq b$ where the AlO_6 octahedra are rotated about a [101] axis. Our sample was always single domain and most measurements were carried out in the (010) zone. The angle between the [100] and [001] axes is $\beta = (90.34 \pm 0.02)°$. Below $T_c = 151$ K the crystal twins about the [101] axis in a monoclinic structure. This twinning phenomenon enables one to measure the strains accompanying the 151-K phase transition with considerable accuracy. We shall discuss this in detail shortly. The lattice constants and angles are again shown in Fig. 3. By 77 K the crystal is very close to being tetragonal; it is noteworthy that it is the c axis and *not* the b axis which becomes the unique

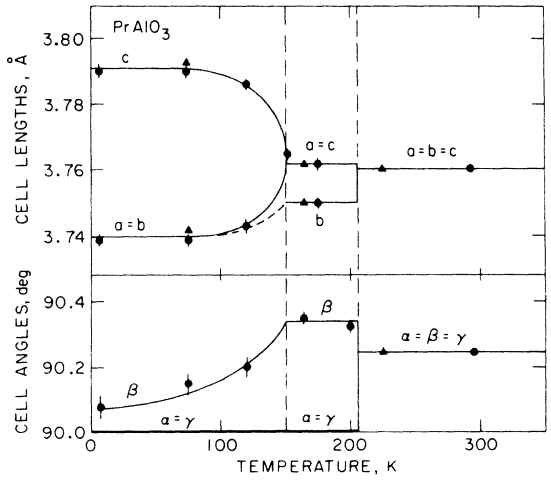

FIG. 3. Temperature variation of the perovskite unit-cell parameters determined by powder diffraction (solid triangles) and single-crystal measurements (solid circles).

axis of the tetragonal phase. It should also be noted that at 4.2 K there is a small but significant deviation of the β angle from 90°, $\beta = (90.07 \pm 0.03)°$; thus $PrAlO_3$ never actually attains a perfect $SrTiO_3$ structure.[37]

Before discussing the twinning angle measurements below 151 K, we consider first our expectations based on the Harley *et al.*[20] model as discussed above, in this model the AlO_6 rotation axis moves continuously from a [101] to a [001] axis below 151 K. The concomitant strains thus may be simply deduced from Eq. (1). For $Q_x = Q \sin\theta$, $Q_z = Q \cos\theta$, and $Q_y = 0$, minimization of U with respect to the $e_{\alpha\beta}$ gives

$$e_{yy} = \frac{-B_e Q^2}{C_{11} - C_{12}}, \quad e_{zz} = \frac{B_e Q^2}{C_{11} - C_{12}} (3\cos^2\theta - 1),$$

$$e_{xx} = \frac{B_e Q^2}{C_{11} - C_{12}} (3\sin^2\theta - 1). \tag{5}$$

This then gives immediately

$$e_{zz} - e_{xx} = \frac{c}{a} - 1 = \frac{3 B_e Q^2}{C_{11} - C_{12}} \cos 2\theta. \tag{6}$$

We now consider the geometry of the twinning. Above T_c the sample is single domain with the AlO_6 octahedra rotated about, say, [101] so that $a = c$ and [101] and [10$\bar{1}$] are exactly perpendicular. This gives rise to a single sharp (202) Bragg peak as illustrated in Fig. 4. Below T_c from Eq. (6) one has $a \neq c$; however, in separate domains the rota-

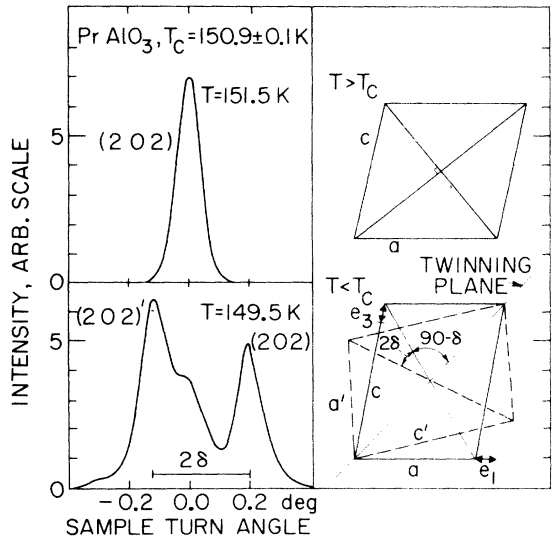

FIG. 4. Illustration of the twinning in the (10$\bar{1}$) planes that is observed below 150.9 K. The angle 2δ between the (101) planes in twinned crystallites can be measured directly from the rocking curves as seen on the left-hand side.

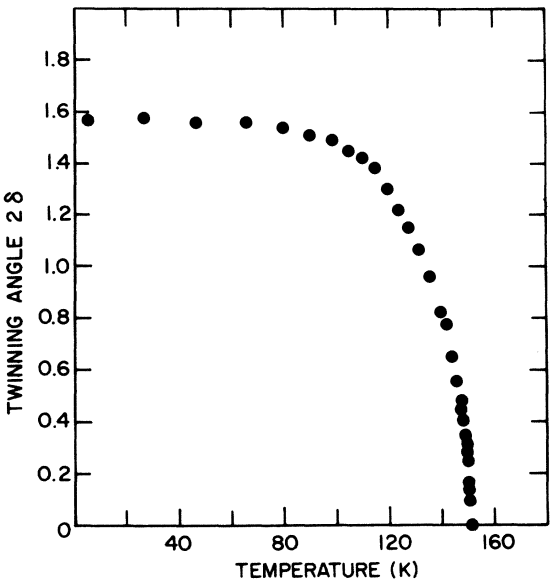

FIG. 5. Measured twinning angle as a function of temperature.

tion axis may move towards [100] or [001]. This gives rise to the twinning pattern illustrated in Fig. 4. From trivial geometrical considerations it follows that

$$\delta \sim \sin\delta = c/a - 1 = e_{zz} - e_{xx} \tag{7}$$

and that in the ideal case the twinning pattern results in two-peaked rocking curves with peak separation 2δ. In general, however, more complicated line profiles result due to increasing mosaic and twinning about both (101) and $(10\bar{1})$. Nevertheless, as illustrated in Fig. 4, the over-all pattern is dominated by two peaks separated by 2δ. Measurements can be made as close as 0.15 K from $T_c = 150.9$ K which allows for an accurate determination of the critical behavior of the strain order parameter. The results for the strain are shown in Fig. 5. We shall discuss in detail the behavior of $e_{zz} - e_{xx}$ as an order parameter including its critical behavior in Sec. IV.

It is evident from Fig. 5 that the strain results are consistent with Eq. (6) assuming that θ varies from 45° to 0° between 151 and 4.2 K, in agreement with the Harley *et al.* hypothesis. We should emphasize, however, that the crystallography shows clearly that at 100 K the crystal structure is *not* tetragonal in contradiction with their claims. We should note that since this work was completed, Cohen *et al.*[22] have measured θ directly via impurity EPR. We shall discuss their results also in Sec. IV. Values for the elastic constants $C_{11} - C_{12}$ and C_{44} together with the strain-rotation coupling constants B_t, B_e are given in Table I.

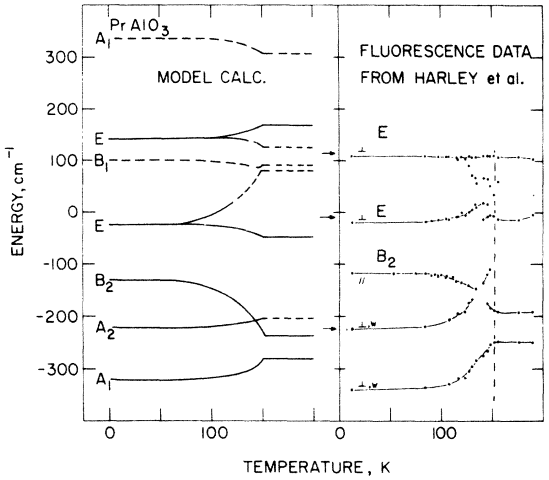

FIG. 6. Crystal field splittings of the lowest levels of the $Pr^{3+}(4f^2)^3H_4$ multiplet as a function of temperature. The right-hand side gives the experimental results of Harley *et al.* (Ref. 20). The dots give the position of peaks in fluorescence originating from the $^3P_0$ level, $\parallel$, $\perp$ denote the polarization in the D_{2d} phase with respect to the unique axis and w denotes a weak transition. The arrows give the position of electronic Raman scattering transitions at 80 K. The left-hand side gives the result of crystal-field calculations as described in Section III B.

The only apparent caveat in the above description of the crystallography is that from Eq. (5) one expects $(c-b)_{T=151\,\mathrm{K}} = \frac{1}{2}(c-a)_{T=0}$ whereas the numerical factor is more like $\frac{1}{4}$. This may indicate that the b lattice constant is not adequately described by Eq. (5) for reasons which we do not fully understand.

B. Crystal fields

1. *Measurements*

Extensive crystal-field spectroscopy in $PrAlO_3$ has been reported by Finkman, Cohen, and Van Uitert[38] and by Harley *et al.*[20] The following discussion is based mainly on the data of Harley *et al.* As discussed in Sec. II, Harley *et al.* have performed detailed Raman scattering and fluorescence measurements of the crystal-field levels of the $Pr^{3+}4f^2$-$^3H_4$ multiplet. Their fluorescence results together with the Raman measurements are summarized in Fig. 6. As is evident in the figure, the crystal-field levels change markedly as a function of temperature, especially between 100 and 151 K. It is, of course, just the lowering of the crystalline electric field (CEF) ground-state energy which accounts for the 151-K transition. It is our main purpose in this section to present a simple microscopic crystal-field model to explain these results. First, however, we review in detail the

results in the tetragonal phase, and we present inelastic neutron scattering crystal-field measurements.

For $T \lesssim 80$ K the point symmetry of the Pr^{3+} site is very nearly D_{2d}. For convenience we reproduce in Table II the character table and transformation properties for the point groups D_{2d} and C_{2v}. The D_{2d} axes in terms of perovskite axes at the Pr^{3+} site are z: [001], x: [110], and y: [1$\bar{1}$0], while the C_{2v} axes are z: [10$\bar{1}$], x: [101], and y: [010] with the AlO_6 octahedra rotated about [101]. The decomposition of the Pr^{3+} $J=4$ manifold in the various principal symmetries is given in Table III. In D_{2d} symmetry there are two doublets and five singlets: $J=4 \rightarrow 2E+2A_1+A_2+B_1+B_2$. As may be seen from Table II, the E and B_2 levels are electric-dipole active and hence may be readily identified in fluorescence. The remaining levels are also present in the fluorescence spectra, but they are much weaker and concomitantly much more difficult to identify unambiguously. Combining all existing data, we give in Table IV our best estimate of the CEF energies and symmetries. At the present time both the B_1 and upper A_1 levels are somewhat uncertain, whereas we regard the other levels as well determined. The only major disagreement between Table IV and Harley *et al.* is the labeling of the first excited state at 117 cm^{-1}. We discuss this apparent conflict after presenting our own CEF experimental results.

Neutron crystal-field spectroscopy has recently been recognized as a powerful tool in the study of crystal fields, especially in metals.[39] The magnetic neutron scattering cross section[40] at small momentum transfers for an assemblage of N noninteracting ions is given by

$$\frac{d^2\sigma}{d\Omega_f d\omega_f} = N\left(\frac{1.91e^2}{2mc^2}g_J\right)^2 f^2(\vec{K})\frac{k_f}{k_i}\sum_{n,m}\rho_n|\langle n|\vec{J}_\perp|m\rangle|^2\delta\left(\frac{E_n-E_m}{\hbar}-\omega\right), \tag{8}$$

when $|n\rangle$, $|m\rangle$ are states belonging to a given J multiplet, $\vec{J}_\perp$ is the component of the total angular momentum operator perpendicular to the scattering vector $\vec{K}$, and the remaining symbols have their usual meaning. The important features of Eq. (8) are that the selection rules are those of simple magnetic dipole spectroscopy and that from the geometry of $\vec{J}_\perp$ it is possible to determine the spatial symmetries involved in the transition. In $PrAlO_3$, below 80 K only the A_1 ground level is appreciably populated. Thus, from Table II, it is evident that the allowed transitions are A_1-A_2 via J_z and A_1-E via J_x, J_y. A typical spectrum is shown in Fig. 7. Between 10 and 50 meV there are two prominent transitions, a strong one at ~14.5 meV = 117 cm^{-1} and a somewhat weaker transition at ~40 meV = 322 cm^{-1} (the sharp feature at 28 meV arises from a $\frac{1}{2}\lambda$ process). Measurements as a function of the wave vector show that the intensities of these two transitions follow the $4f$ electronic form factor squared, $f^2(\vec{K})$, thus verifying that these are crystal-field transitions. By application of a magnetic field, the sample can be made single domain.[18] From the geometrical behavior of the intensities it is then possible to show that the 14.5-meV transition is induced by J_z. This then uniquely identifies this transition as A_1-A_2. Its energy is in close agreement with that for the ground state—first excited-state transition seen by Harley *et al.*[20] via Raman scattering and fluorescence. Harley *et al.*, however, have identified this transition as A_1-B_1. We believe that this is incorrect and that they are simply observing the A_1-A_2 transition in Raman scattering via the antisymmetric pseudovector scattering mechanism for electronic transitions.[41] Our assignment is also supported by the detailed crystal-field calculations to be described shortly. The transition at ~40 meV in Fig. 7 is then A_1-E and both the energy and identification agree with that of Harley *et al.* With somewhat

TABLE II. Character tables and selection rules for groups D_{2d} and C_{2v}.

$D_{2d}(42m)$			E	C_2	$2S_4$	$2C_2'$	$2\sigma_d$
x^2+y^2, z^2		A_1	1	1	1	1	1
	J_z	A_2	1	1	1	−1	−1
x^2-y^2		B_1	1	1	−1	1	−1
xy	z	B_2	1	1	−1	−1	1
(xz, yz)	(x, y) (J_x, J_y)	E	2	−2	0	0	0

$C_{2v}(2mm)$			E	C_2	σ_v	σ_v'
x^2, y^2, z^2	z	A_1	1	1	1	1
xy	J_z	A_2	1	1	−1	−1
xz	$J_y x$	B_1	1	−1	1	−1
yz	$J_x y$	B_2	1	−1	−1	1

TABLE III. Decomposition of $J=4$ in the principal symmetries in $PrAlO_3$.

$Pr^{+3}\ ^3H_4$; 9 levels				
O_h	E_g	T_{1g}	T_{2g}	A_1
$D_3[111]$ [a]	E	A_2+E	A_1+E	A_1
$C_{2v}[101]$ [a]	A_1+B_1	$A_2+B_1+B_2$	$A_1+A_2+B_2$	A_1
$D_{2d}[001]$ [a]	A_1+B_2	A_2+E	B_1+E	A_1

[a] Unique axis.

TABLE IV. Energy levels and CEF parameters at 4.2 K—D_{2d} symmetry.

Label	Experiment (cm^{-1})	Theory Model 1 (using $NdAlO_3$ parameters with $\alpha=\frac{2}{3}$)	Theory Model 2 (fitted to definitely identified levels)	Theory Model 3 (fitted to all levels)
A_1	0	0	0	0
A_2	117	181	93	134
B_2	224	180	192	182
E	319	323	312	273
B_1	(356)? [a]	445	443	391
E	445	553	462	494
A_1	(780)? [a]	883	657	753
CEF parameters		(cm^{-1})	(cm^{-1})	(cm^{-1})
	B_2	795	770 ± 70	770 ± 110
	B_4	−650	−70 ± 260	−540 ± 200
	B_6	−920	−650 ± 80	−740 ± 90

[a] More recent measurements and calculations by Lyons *et al.* (Ref. 55) have cast doubt on the location of the B_1 level at 356 cm^{-1} and they indicate that the upper A_1 level is at 925 cm^{-1}.

less certainty, we have also observed the other A_1-E transition at 54 ± 1 meV ≃ 440 cm^{-1}.

We consider briefly both the dispersion and temperature dependence of these excitations. Measurement of the dispersion of the A_1-A_2 and A_1-E excitations were carried out in a number of directions as a function of temperature. Typical dispersion curves are shown in Fig. 8. The A_1-A_2 mode is found to be absolutely flat in all principal directions. As the temperature is raised from 77 to 151 K, the excitation increases gradually in energy from 14.5 to ~16.7 meV in agreement with the fluorescence results of Harley *et al.* as shown in Fig. 6. By 151 K the A_1-A_2 mode has become extremely broad and hence nearly unobservable. The dispersion of the A_1-E modes at 77 K are shown in Fig. 8. In the [101] direction the over-all dispersion of the lowest A_1-E mode is about 1.5 meV. This dispersion originates in the exciton-phonon interaction as we shall discuss in Sec. IV. As the temperature is increased, the energy of the lower E level decreases to about 34 meV and the mode becomes extremely broad. This latter result is again in agreement with the fluorescence measurements.

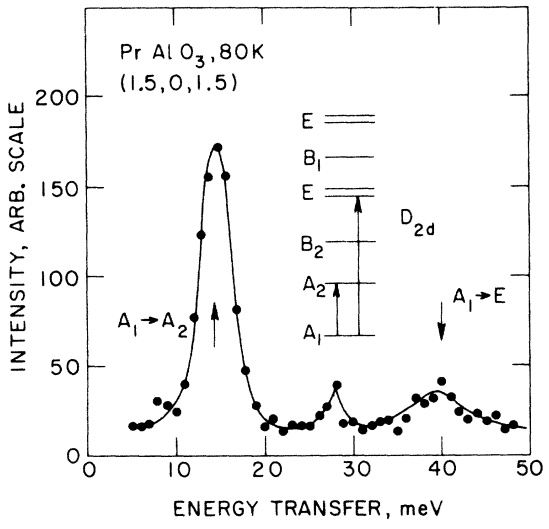

FIG. 7. Typical inelastic neutron scan at 77 K showing two magnetic dipole active crystal-field transitions. The basis for the symmetry assignments is discussed in the text.

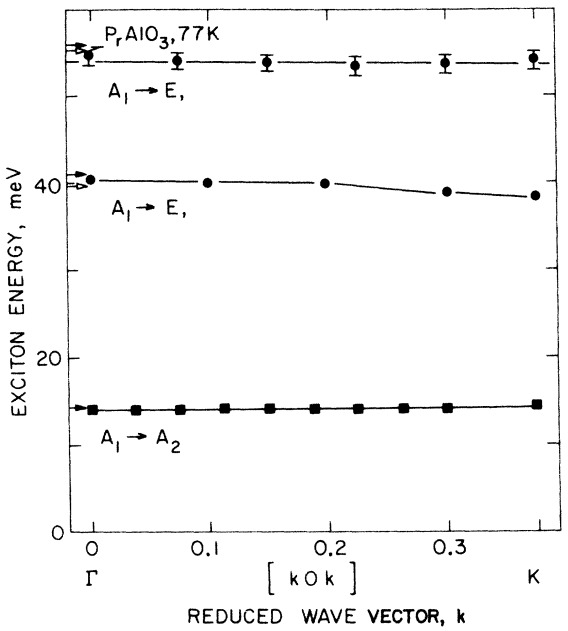

FIG. 8. Dispersion relations in the [$k0k$] direction of the A_1-A_2 and A_1-E excitons at 77 K.

2. *Theory*

We now discuss the crystal-field theory for Pr^{3+} in $PrAlO_3$. In the following discussion we shall consider exclusively the $(4f^2)$-$^3H_4$ manifold; in particular, we shall ignore all perturbative effects of the $^3H_5$ manifold[42] at 2100 cm^{-1}. This may produce quantitative errors in calculated CEF energies by as much as 10% but since our discussion will be primarily semiquantitative, such errors will be within the uncertainties arising from other approximations.

The theory and empirical behavior of crystal fields in rare-earth insulators has been the subject of extensive investigation over several decades.[42,43] Here we shall lean heavily on the accumulated "wisdom" obtained from these studies. As long as we are concerned only with the lowest $J=4$ manifold, the crystal-field Hamiltonian may be written

$$\mathcal{H}_{\mathrm{CEF}} = \sum_{\substack{n=2,4,6 \\ m=-n;n}} B_n^m \chi_n \tilde{O}_n^m(J), \tag{9a}$$

where the $\tilde{O}_n^m(J)$ are angular momentum operator equivalents[44] corresponding to $[4\pi/(2n+1)]^{1/2} \times Y_n^m(\theta,\varphi)$. Matrix elements of the $\tilde{O}_n^m$ have been tabulated by Birgeneau.[45] The χ_n are reduced matrix elements tabulated by Elliott and Stevens[46] and the B_n^m are the crystal-field parameters. The number of independent B_n^m, of course, depends on the point symmetry at the rare-earth site. For the point symmetries encountered in $PrAlO_3$ the numbers of such parameters are the following: O_h, 2; D_3, 6; C_{2v}, 9; C_s, 15; D_{2d}, 5. Since there are in all only nine levels in the $^3H_4$ manifold, it is clear that one will have to make some simplifying approximation to arrive at even an empirical description of the crystal-field levels.

The simplest theory for the B_n^m is the point-charge model (PCM) as discussed extensively by Hutchings.[47] In the PCM the B_n^m are given by

$$B_n^m = (-)^{m+1}|e|\langle r^n\rangle(1-\sigma_n)\sum_j \frac{q_j}{R_j^{n+1}} Y_n^{-m}(\theta_j,\varphi_j), \tag{9b}$$

where the sum is over all atoms with charge q_j at position (R_j,θ_j,φ_j). Here $\langle r^n\rangle$ is the nth moment of the $4f$ electron distribution and $(1-\sigma_n)$ is the Sternheimer $4f$ shielding factor.[48] The PCM is of course much too naive to describe real crystals.[49] In general, it somewhat overestimates the B_2^m, gives the right order of magnitude for the B_4^m, and grossly underestimates the B_6^m. However, it usually gives the right sign and, most importantly, gives nearly correct ratios $B_n^m/B_n^{m'}$ since the latter are determined predominantly by geometry.[50] Perhaps the best first approximation for the B_n^m for a given crystal is obtained simply by knowing the B_n^m for an isostructural rare-earth compound,[42] the differences being entirely due to the χ_n.

In order to describe the crystal-field splitting in the various phases of $PrAlO_3$, we make the following approximations. Firstly, we assume that the fourth- and sixth-order CEF coefficients are unaffected by the rotations of the AlO_6 octahedra so that we simply take for the B_4^m, B_6^m constant values appropriate to the cubic perovskite structure. This then reduces one from as many as 12 to 2 adjustable parameters, B_4, B_6. Secondly, we assume that the geometry and approximate magnitude of the second-order terms are correctly given by the nearest-neighbor PCM. This then reduces the problem to a conceptually simple but rather tedious algebraic exercise.

We consider separately the effects of the rotations of the AlO_6 octahedra and the concomitant strains. Blount[51] has shown that for a rotation $\vec{Q}=(Q\cos\theta_x, Q\cos\theta_y, Q\cos\theta_z)$ the quadrupole tensor is given by

$$\underline{B}_2 = C\begin{pmatrix} & J_x & J_y & J_z \\ & 3\cos^2\theta_x - 1 & -2\cos\theta_x\cos\theta_y & -2\cos\theta_x\cos\theta_z \\ & -2\cos\theta_x\cos\theta_y & 3\cos^2\theta_y - 1 & -2\cos\theta_y\cos\theta_z \\ & -2\cos\theta_x\cos\theta_z & -2\cos\theta_y\cos\theta_z & 3\cos^2\theta_z - 1 \end{pmatrix}, \tag{10}$$

with

$$C = Ze^2\langle r^2\rangle(1-\sigma_2)\frac{57}{2\sqrt{2}\,a^3}\sin^2 Q,$$

where Ze is the oxygen charge and a is the lattice constant of the perovskite cell. This then may be simply transformed into the form of Eq. (9a).

One obtains a result essentially identical to Eq. (10) for the strain contribution but with

$$\cos\theta_\alpha\cos\theta_\beta \to e_{\alpha\beta} \tag{11}$$

and

$$C = \frac{6}{\sqrt{2}\,a^3} Ze^2\langle r^2\rangle(1-\sigma_2).$$

By minimizing Eq. (1) with respect to the $e_{\alpha\beta}$ one finds that the strains and the AlO_6 rotation angles are related by

$$e_{\alpha\beta} = \frac{B_t}{C_{44}} Q^2 \cos\theta_\alpha \cos\theta_\beta, \quad \alpha \neq \beta$$
$$e_{\alpha\alpha} = \frac{B_e}{C_{11} - C_{12}} Q^2 (3\cos^2\theta_\alpha - 1). \tag{12}$$

Thus the strain quadrupole tensor has the same geometrical structure as Eq. (10) but with a different ratio for the diagonal and off-diagonal terms. It is convenient to combine the strain and rotation contributions in the following form

$$\underline{B}_2 = C' \begin{pmatrix} 3\cos^2\theta_x - 1 & -3\alpha\cos\theta_x\cos\theta_y & -3\alpha\cos\theta_x\cos\theta_z \\ -3\alpha\cos\theta_x\cos\theta_y & 3\cos^2\theta_y - 1 & -3\alpha\cos\theta_y\cos\theta_z \\ -3\alpha\cos\theta_x\cos\theta_z & -3\alpha\cos\theta_y\cos\theta_z & 3\cos^2\theta_z - 1 \end{pmatrix}, \tag{13}$$

where now α is an adjustable parameter which equals $\frac{2}{3}$ for the PCM AlO_6 rotation contributions alone.[51] We shall assume that Eq. (13) applies for all phases in $PrAlO_3$. Although Eq. (13) is PCM based, it is essentially a geometrical result and hence it should hold for more general crystal-field models.

We now consider the crystal fields in $PrAlO_3$ based on the above approximations. The two consequences of Eq. (13) which are of the most practical import are the following:

(a) The field gradients in the rhombohedral and tetragonal phases are simply related by

$$B_2^0(100) = -(1/\alpha) B_2^0(111). \tag{14}$$

(b) For $Q = (Q\sin\theta, 0, Q\cos\theta)$ as in the orthorhombic, monoclinic and tetragonal phases,

$$B_2^0 = B_2 \tfrac{1}{2}(3\cos^2\theta - 1),$$
$$B_2^1 = (3/8)^{1/2} \alpha B_2 \sin 2\theta, \tag{15}$$
$$B_2^2 = (3/8)^{1/2} B_2 \sin^2\theta.$$

Alternatively, the quadrupole tensor may be diagonalized by rotating the z axis in the xz plane through an angle φ determined by

$$\tan 2\varphi = -\alpha \tan 2\theta. \tag{16}$$

The CEF parameters relative to these axes are then

$$B_2^{0\prime} = B_2 \tfrac{1}{2}[\tfrac{1}{2} + \tfrac{3}{2}(\cos^2 2\theta + \alpha^2 \sin^2 2\theta)^{1/2}],$$
$$B_2^{2\prime} = B_2 \tfrac{1}{2}\{\tfrac{1}{2} + \tfrac{3}{2}[1 - (\cos^2 2\theta + \alpha^2 \sin^2 2\theta)^{1/2}]\}. \tag{17}$$

In summary then we take as the crystal-field Hamiltonian in $PrAlO_3$ for the tetragonal, monoclinic, and orthorhombic phases

$$\mathcal{H}_{CEF} = B_2^0 \chi_2 \tilde{O}_2^0 + B_2^1 \chi_2 (\tilde{O}_2^1 - \tilde{O}_2^{-1}) + B_2^2 \chi_2 (\tilde{O}_2^2 + \tilde{O}_2^{-2})$$
$$+ B_4 \chi_4 [\tilde{O}_4^0 + (5/14)^{1/2} (\tilde{O}_4^4 + \tilde{O}_4^{-4})]$$
$$+ B_6 \chi_6 [\tilde{O}_6^0 - (7/2)^{1/2} (\tilde{O}_6^4 + \tilde{O}_6^{-4})], \tag{18}$$

where the B_2^m are given by Eq. (15). There are thence only four fundamental parameters B_2, B_4, B_6, and α and the differences of the CEF splittings in the different phases should then be determined by the AlO_6 rotation axis direction alone.

As a starting point, the CEF parameters for $PrAlO_3$ may be simply taken to be identical to those in $NdAlO_3$. Finkman *et al.*[38] have carried out a detailed crystal-field analysis of $NdAlO_3$, which as we have noted previously, is isostructural with the rhombohedral phase of $PrAlO_3$. From these CEF parameters for $NdAlO_3$, we calculate averaged cubic parameters B_4, B_6. In addition, from the rhombohedral field gradient $B_2^0(111)$ in $NdAlO_3$ we can, via Eq. (14), estimate the tetragonal field gradient $B_2(100)$ appropriate to $PrAlO_3$ in the low-temperature D_{2d} phase. The results so-obtained are listed in Table IV as Model 1. From Table IV it is evident that the crystal-field energies calculated using these parameters are in rather good agreement with the measured values especially considering the fact that we have so-far introduced no adjustable parameters. In an attempt to improve the agreement, we have carried out a standard least-squares analysis, fitting to either just the definitely identified levels (Model 2) or to all levels (Model 3). The results of these fits are also shown in Table IV. The agreement with the measured energies is improved although it is by no means exact. The remaining discrepancies arise from our use of only three rather than the allowed five parameters for D_{2d} symmetry and from the omission of perturbative effects from the $^3H_5$ manifold. We note also that the relative intensities of the A_1-A_2, A_1-E transitions as shown in Fig. 7 are correctly predicted by the above CEF models. The best fit B_2 is in good agreement with the value of B_2 estimated via Eq. (14) with $\alpha = \frac{2}{3}$ from $NdAlO_3$. A simple nearest-neighbor PCM calculation of B_2 using Eqs. (10), (11) with $Q_0 = 9.4°$ and $\epsilon_{zz} - \frac{1}{2}(\epsilon_{xx} + \epsilon_{yy}) = 0.0135$, gives $B_2(\mathrm{PCM}) = 650$ cm^{-1} in good agreement with the best fit value. Finally, B_4 is rather poorly determined by the fits while B_6 is comparable with, but somewhat smaller in magnitude than, the corresponding value in $NdAlO_3$.

We now consider the temperature dependence of the Pr^{3+} crystal-field levels. As discussed extensively in the previous sections, in the Harley *et al.*[20] model as the temperature is increased

from 77 to 151 K the AlO_6 rotation axis θ moves continuously from the [001] to [101] direction. The actual relationship of θ vs T can be estimated from the strain data shown in Fig. 5 using Eq. (6) to transform the $e_{zz} - e_{xx}$ to θ. B_2, B_4, B_6 have been determined by the fits to the D_{2d} data so that α remains the only adjustable parameter. We show in Fig. 6 a typical calculated temperature dependence of the energy levels using the parameters of Model 2 with $\alpha = 1$. The choice $\alpha = 1$ corresponds physically to assuming that as θ varies from 0 to 45°, the field gradient rotates from 0 to −45° while remaining axial and constant in magnitude [see Eqs. (16) and (17)]. From Fig. 6 it is evident that there is semiquantitative agreement between experiment and this simple theory at all temperatures. We have thus succeeded in reproducing at least the principal features of the apparently very complicated behavior of the CEF levels over a wide range of temperatures using only four adjustable parameters, all of which could be reasonably estimated without recourse to the experimental data. Considering the fact that at all intermediate temperatures there are 15-independent CEF parameters, we consider this to be a notable success of the theory.

Physically then, the 151-K phase transition in $PrAlO_3$ involves the AlO_6 rotation axis itself moving continuously from the [101] to the [001] direction. This in turn causes the principal component of the electric field gradient tensor at the Pr^{3+} site to rotate from $[10\bar{1}]$ to [001]; the field gradient stays nearly constant in magnitude and axial in form. As discussed previously, the decrease in the Pr^{3+} ground-state energy as a result of this reorientation of the field gradient compensates for the cost in lattice energy involved in orienting the AlO_6 octahedra rotation axis along one of the perovskite axes. This is, in fact, a classic illustration of the cooperative Jahn-Teller effect as we shall discuss extensively in Sec. IV.

IV. 151-K TRANSITION AS A COOPERATIVE JAHN-TELLER TRANSITION

A. General considerations

As discussed in the Introduction to the paper, the cooperative Jahn-Teller effect in rare-earth insulators has been extensively explored in a series of papers by Elliott and co-workers.[4,10] The reader is referred to their papers, and in particular to Ref. 4, for a detailed discussion of the theory. In this subsection we reproduce their results which are essential for $PrAlO_3$. We consider a simple two-level system with ground state A_1 and first excited state B_1 where A_1, B_1 are representations of the point group at the rare-earth site. We assume further that only coupling to displacements of B_1 symmetry are important. The choice of labels A_1, B_1 is, of course, arbitrary. The crystal Hamiltonian thus may be written

$$\mathcal{H} = \mathcal{H}_{\text{lattice}} + \sum_l \epsilon O_{A_1}(l) + \sum_{i,l} \zeta_{B_1}(i) Q_{B_1}(i) O_{B_1}(l) , \tag{19}$$

where $Q_{B_1}(i)$ and O_{B_1} are B_1 displacement and electric quadrupole angular momentum operators, respectively. The first term represents the noninteracting phonons, the second term the static crystal field, and the third the quadrupole-displacement interaction.

In order to carry out calculations using Eq. (19) two transformations are introduced. Firstly, it is convenient to replace O_{A_1}, O_{B_1} by Pauli spin operators σ_x, σ_z, which operate on the basis $|1\rangle$, $|-1\rangle$. The eigenstates are then defined by $|A_1\rangle \rightarrow (1/\sqrt{2})(|1\rangle - |-1\rangle)$, $|B_1\rangle \rightarrow (1/\sqrt{2})(|1\rangle + |-1\rangle)$ with $\langle B_1|\sigma^x|A_1\rangle = 1$; we assume that the proportionality factors $\langle B_1|O_{B_1}|A_1\rangle$, $\langle A_1|O_{A_1}|A_1\rangle$ are absorbed in ζ and ϵ, respectively. Secondly, it is necessary to Fourier transform Eq. (19) in order to work with normal mode operators. With the assumption of one atom per unit cell, the lattice Fourier transforms are

$$\sigma^\alpha(\vec{k}) = \frac{1}{\sqrt{N}} \sum_l \sigma^\alpha(l) e^{i\vec{k}\cdot\vec{R}(l)} \tag{20}$$

and the Jahn-Teller term becomes

$$\mathcal{H}_{J-T} = \sum_{n,\vec{k}} \xi_n(\vec{k})[C_n^\dagger(-\vec{k}) + C_n(\vec{k})]\sigma^z(\vec{k}) , \tag{21}$$

where the $C_n(\vec{k})$ are the usual destruction operators for phonons of wave vector $\vec{k}$ belonging to branch n. In our simplified model the branch index n must be compatible at $\vec{k} = 0$ with the site symmetry B_1. As discussed by Elliott *et al.* the full Hamiltonian for the coupled electron-phonon system then becomes

$$\begin{aligned}\mathcal{H} = \sum_{n,\vec{k}} \{&[C_n^\dagger(\vec{k})C_n(\vec{k}) + \tfrac{1}{2}]\hbar\omega(\vec{k}) \\ &+ \xi_n(\vec{k})[C_n^\dagger(-\vec{k}) + C_n(\vec{k})]\sigma_z(\vec{k})\} \\ &- \epsilon\sqrt{N}\sigma^x(0) - \eta e_{B_1}\sqrt{N}\sigma^z(0) ,\end{aligned} \tag{22}$$

where the first term represents the phonon energies in the harmonic approximation, the second term is the electron-phonon coupling and the term in ϵ gives the initial crystal-field splitting. The final term represents the coupling to the macro-

scopic strains of symmetry B_1. The strain is treated separately since for periodic boundary conditions $\xi_a(0)=0$ for the acoustic phonons.[52] In molecular-field theory, the strain is simply proportional to $\langle\sigma^z\rangle$. Thus the final term in Eq. (22) may be replaced by $-\mu\langle\sigma^z\rangle\sum_l\sigma^z(l)$. The essential step in solving Eq. (22) is to introduce the transformation

$$\gamma_n^\dagger(\vec{k})=C_n^\dagger(\vec{k})+[\xi_n(\vec{k})/\hbar\omega_n(\vec{k})]\sigma^z(\vec{k})\,. \tag{23}$$

The Hamiltonian, Eq. (22), becomes

$$\begin{aligned}\mathcal{H}=&\sum_{n,\vec{k}}[\gamma_n^\dagger(\vec{k})\gamma_n(\vec{k})+\tfrac{1}{2}]\hbar\omega_n(\vec{k})\\&-\frac{1}{2}\sum_{\vec{k}}J(\vec{k})\sigma^z(\vec{k})\sigma^z(-\vec{k})-\epsilon\sqrt{N}\sigma^x(0)\\&-\mu\langle\sigma^z\rangle\sqrt{N}\,\sigma^z(0)\,,\end{aligned} \tag{24}$$

where

$$\begin{aligned}&J(\vec{k})=\sum_n J_n(\vec{k})\,,\quad J_n(\vec{k})=K_n(\vec{k})-\frac{1}{N}\sum_{\vec{k}}K_n(\vec{k})\,,\\&K_n(\vec{k})=2\xi_n^2(\vec{k})/\hbar\omega_n(\vec{k})\,.\end{aligned} \tag{25}$$

One recognizes immediately the final part of $\mathcal{H}$ in Eq. (24) as just the Hamiltonian of the Ising model in a transverse field which, as we have noted previously, has been the subject of extensive theoretical investigation.[4,12-16] Physically, the Ising interaction corresponds to an effective quadrupole-quadrupole interaction mediated via the phonons, the strain contribution then being equivalent to an infinite range interaction.

As the first approximation for the static properties,[4] one ignores the noncommutation of the displaced oscillator and the transverse field parts of Eq. (24) and then simply treats the Ising model in a transverse field via molecular-field theory. Here we assume that the effective interaction is ferroquadrupolar so that the ordering occurs at $k=0$. The essential results are the following.

(a) T_c is defined by

$$\frac{\epsilon}{J(0)+\mu}=\tanh\left(\frac{\epsilon}{kT_c}\right). \tag{26}$$

Thus there can be no transition if $|\epsilon|>|J(0)+\mu|$.

(b) Below T_c the order parameter is given by

$$\langle\sigma^z\rangle=\frac{[J(0)+\mu]\langle\sigma^z\rangle}{W}\tanh\left(\frac{W}{kT}\right), \tag{27}$$

where

$$W=(\{[J(0)+\mu]\langle\sigma^z\rangle\}^2+\epsilon^2)^{1/2} \tag{28}$$

and

$$\langle\sigma^x\rangle=(\epsilon/W)\tanh(W/kT)\,. \tag{29}$$

Here $2W$ is the splitting between the doublet levels in the ordered phase.

(c) If the strain elastic energy is taken as $\frac{1}{4}NV_0(C_{11}-C_{12})e_{B_1}^2$, then the equilibrium value of the strain is

$$\langle e_{B_1}\rangle=4\eta\langle\sigma^z\rangle/V_0(C_{11}-C_{12})\,. \tag{30}$$

Similarly, there is a displacement in each $k=0$ optic-phonon mode which couples to the operator $\sigma^z(0)$; the magnitude of the displacement in terms of the local coordinate $Q_n(l)$ of the $k=0$ optic mode n is

$$\langle Q_n(l)\rangle=-\zeta_{B_1}^n\langle\sigma^z\rangle/M\omega_n^2(0)\,. \tag{31}$$

The results for the dynamics are rather more complicated. Again, if one ignores the noncommutation of the first and second parts of Eq. (24), then above T_c, the electronic excitation has a dispersion relation which in a mean-field RPA treatment is given by

$$\hbar\omega_E(\vec{k})=2\epsilon\left[1-\frac{J(\vec{k})}{\epsilon}\tanh\left(\frac{\epsilon}{k_BT}\right)\right]^{1/2}. \tag{32}$$

We call this excitation a *quadrupole exciton* since physically it involves a wavelike modulation of the rare-earth electric quadrupole moment. For ferroquadrupolar coupling, $\hbar\omega_E(0)$ will go to zero at the temperature T_c given by Eq. (26). Thus in the approximation, the phase transition is a simple soft-mode phase transition with the electronic mode the soft mode of the system. It is evident, however, that if there is linear coupling to a symmetry compatible acoustic-phonon mode (and at $k=0$ the corresponding strain) then the acoustic phonon and not the electronic mode must be the soft mode of the system. Such a result is in fact found if one treats the full Hamiltonian Eq. (24) and not just the Ising-model-in-a-transverse-field part. A general treatment has been given by Elliott *et al.*[4] For our purposes it is adequate to reproduce the results which are appropriate for low energies and long wavelengths. Elliott *et al.* find that the mixed acoustic phonon-exciton dispersion relations are given by

$$\begin{aligned}\tfrac{1}{4}\hbar^2\omega_e^2(\vec{k})=&\{[J(0)+\mu]\langle\sigma^z\rangle\}^2\\&+\epsilon\{\epsilon-[J_0(\vec{k})-\mu_a]\langle\sigma^x\rangle\}\,,\end{aligned} \tag{33}$$

$$\frac{\omega_p^2(\vec{k})}{\omega_a^2(k)}=\frac{\epsilon-[J_0(k)+K_a(\vec{k})-\mu_a]\langle\sigma^x\rangle}{\epsilon-[J_0(k)-\mu_a]\langle\sigma^x\rangle}\,,\quad T\geq T_c \tag{34}$$

where $\langle\sigma^x\rangle$, $\langle\sigma^z\rangle$ are given by Eqs. (27) and (29), $\omega_e(\vec{k})$ and $\omega_p(\vec{k})$ are the renormalized exciton and phonon energies, $\omega_a(\vec{k})$ is the acoustic phonon energy in the absence of the exciton coupling,

$J_0(\vec{k})$ is the optic-mode contribution to $J(\vec{k})$, and $K_a(\vec{k}) - \mu_a$ is the acoustic-mode contribution. Here $\lim_{k\to 0} K_a(\vec{k}) = \mu$, the strain contribution. From Eq. (34) one sees that $\lim_{k\to 0} \omega_p^2(\vec{k})/\omega_a^2(\vec{k}) = 0$ at a temperature defined by

$$\tanh\frac{\epsilon}{kT_c} = \lim_{k\to 0}\frac{\epsilon}{J_0(\vec{k}) + K_a(\vec{k}) - \mu_a} = \frac{\epsilon}{J_0(0) + \mu}\,, \tag{35}$$

which is again just the molecular-field result [Eq. (26)] for T_c. Thus in this treatment as expected the acoustic phonon is the soft mode of the system.

It is evident that from a measurement of the coupled dispersion relations one should be able to obtain a great deal of physical information. In particular, one may deduce $J_0(\vec{k}) - \mu_a$ and $K_a(\vec{k})$ separately; these in turn are simply related to the wave-vector-dependent electron-phonon coupling.

We now apply these results to $PrAlO_3$.

B. Jahn-Teller Hamiltonian and order parameters in $PrAlO_3$ at 151 K

The low-lying crystal-field levels in the various phases of $PrAlO_3$ are shown schematically in Fig. 9. These are calculated with the parameters of Model 2 with $\alpha = 1$. We now confine our attention to the 151-K transition which is from C_{2v} to C_s and, at completion, to D_{2d} symmetry at the Pr^{3+} site. In the C_{2v} phase with $\alpha = 1$ the crystal-field Hamiltonian may be simply written

$$\mathcal{H}_{\rm CEF} = B_2\chi_2\tilde{O}_2^0 + B_4\chi_4(-\tfrac{1}{4})[\tilde{O}_4^0 - \sqrt{10}(\tilde{O}_4^2 + \tilde{O}_4^{-2}) - \tfrac{3}{7}\sqrt{(35/2)}(\tilde{O}_4^4 + \tilde{O}_4^{-4})]$$
$$+ B_6\chi_6(-\tfrac{13}{8})[\tilde{O}_6^0 + (\sqrt{105}/26)(\tilde{O}_6^2 + \tilde{O}_6^{-2}) - \tfrac{5}{13}\sqrt{(7/2)}(\tilde{O}_6^4 + \tilde{O}_6^{-4}) + (\sqrt{231}/26)(\tilde{O}_6^6 + \tilde{O}_6^{-6})]\,, \tag{36}$$

where the local C_{2v} axes, z': [10$\bar{1}$], x': [101], and y': [010], are chosen as the CEF axes of quantization. For an infinitesimal rotation φ of the field gradient in the $x'z'$ plane, the Hamiltonian becomes

$$\mathcal{H}_{\rm CEF} = B_2\chi_2[\tfrac{1}{2}(3\cos^2\varphi - 1)\tilde{O}_2^0 - \sqrt{(3/8)}\,\sin 2\varphi(\tilde{O}_2^1 - \tilde{O}_2^{-1}) + \sqrt{(3/8)}\,\sin^2\varphi(\tilde{O}_2^2 + \tilde{O}_2^{-2})] + B_4\cdots + B_6\circ\circ\circ\,, \tag{37}$$

so that the only term linear in φ is

$$\mathcal{H}_\varphi = B_2\chi_2\sqrt{(3/8)}\,\sin 2\varphi(\tilde{O}_2^{-1} - \tilde{O}_2^1)\,. \tag{38}$$

The angular momentum operator $\tilde{O}_2^{-1} - \tilde{O}_2^1 \sim J_{x'}J_{z'} + J_{z'}J_{x'}$ which from Table II transforms like B_1. We therefore write

$$O_2^{B_1} = \frac{1}{\sqrt{2}}(\tilde{O}_2^{-1} - \tilde{O}_2^1)\,. \tag{39}$$

Now in the C_{2v} phase[20] the R_{25} phonons of the cubic phase split into an A_1 mode at ~230 cm^{-1}, a B_1 mode and an A_2 mode. From the Raman scattering spectra we infer that the latter two modes are at 81 and 45 cm^{-1}, respectively. The eigenvector of the B_1 optical-phonon mode corresponds to a staggered rotation around the [10$\bar{1}$] axis; thus a condensation of the B_1 optic mode gives a resultant axis of staggered rotation at an angle $\theta_{[101]}$ from [101] determined by $\theta_{[101]} \sim \langle Q_{B_1}^0\rangle/Q_0$ where Q_0 is the over-all angle of rotation. From Eq. (16) one has $\varphi = -\theta_{[101]}$. Thus Eq. (37) may be written, for small φ,

$$\mathcal{H} = -B_2\chi_2\sqrt{3}\,\frac{1}{Q_0}Q_{B_1}^0 O_2^{B_1}$$
$$= \zeta_{B_1}^0 Q_{B_1}^0 O_2^{B_1}\,, \tag{40}$$

where

$$\zeta_{B_1}^0 = -B_2\chi_2\sqrt{3}\,(1/Q_0)\,.$$

The more general result for $\alpha \neq 1$ may be similarly derived from Eqs. (16) and (17). There will be a similar term arising from the coupling to the strain $e_{x'z'}$ which in perovskite axes is $e_{zz} - e_{xx}$. This latter in turn is just the $k = 0$ limit of the

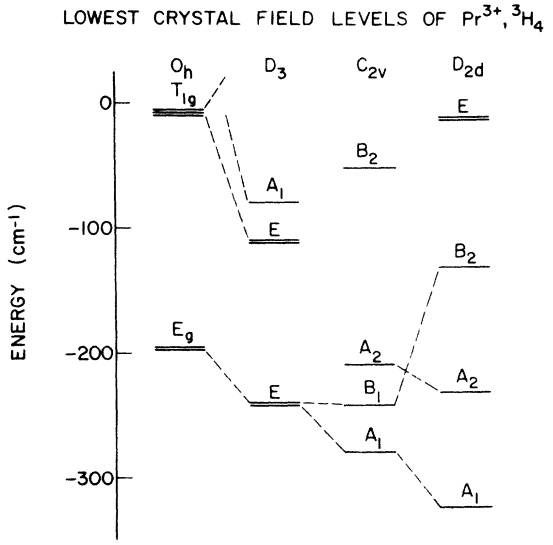

FIG. 9. Lowest crystal-field levels of the Pr^{3+}, $^3H_4$ multiplet in the various principal symmetries of $PrAlO_3$. The levels are calculated using the parameters of Model 2 from Table IV with $\alpha = 1$. The symmetry identifications have been experimentally confirmed for the D_{2d} phase only.

T[101] (perovskite) acoustic phonon. It should be emphasized that the normal phonon modes in the orthorhombic phase have a mixed character in terms of perovskite phonon eigenvectors so that, for example, the acoustic-phonon coupling constants will contain contributions from both the internal and external strain [see Eq. (1)]. In terms of lattice-Fourier transform operators the Jahn-Teller Hamiltonian may be written

$$\mathcal{H}_{J-T} = \sum_{\vec{k}} [\zeta^a_{B_1}(\vec{k}) Q^a_{B_1}(\vec{k}) O_2^{B_1}(-\vec{k}) + \zeta^0_{B_1}(\vec{k}) Q^0_{B_1}(\vec{k}) O_2^{B_1}(-\vec{k})] . \quad (41)$$

Furthermore, among the levels which are thermally populated at ~151 K H_{J-T} will only couple the A_1 state to the B_1 state; that is, it only has matrix elements within the original cubic E_g doublet so that the A_2 level may be taken to be essentially inert. We should note that the actual ordering and separation of the A_1 and B_1 levels depends sensitively on the explicit choice of CEF parameters. However, none of the following discussion is altered by an interchange of the identifications of the two lowest levels in the C_{2v} phase. It is evident, therefore, that above 151 K in the orthorhombic phase, $PrAlO_3$ corresponds very closely to the idealized model for the cooperative Jahn-Teller effect discussed in Sec. IV A. We have the additional simplification that it should involve only one acoustic phonon and one optical phonon.

We consider first the results for the various order parameters below 151 K in $PrAlO_3$. Measurements of the strain order parameter $e_{zz} - e_{xx}$ (perovskite units) have already been presented in Sec. III A and are shown in Fig. 5. The electronic order parameter may be readily deduced from the fluorescence data[20] shown in Fig. 6. From Eq. (28) one has

$$\frac{\langle \sigma_z \rangle_T}{\langle \sigma_z \rangle_0} = \left(\frac{W^2(T) - \epsilon^2}{W^2(0) - \epsilon^2} \right)^{1/2} . \quad (42)$$

The internal displacement order parameter $\langle Q^0_{B_1} \rangle$ has been measured via EPR by E. Cohen *et al.*[22] As discussed by these authors, since the coupling to the phonons is of the form $Q_z^2 - Q_x^2$, it is necessary to take as the optical-phonon order parameter $\sin 2\theta_{[101]}$ rather than $\theta_{[101]}$ itself. The experimental results for the normalized electronic, strain and optical-phonon order parameters (O.P.) are shown together in Fig. 10(a). It is evident that these various quantities are in remarkably good absolute agreement with each other. This represents an important confirmation both of our model for $PrAlO_3$ and of the basic physical assumptions in the existing theory of the CJTE.

We may also calculate theoretically the order parameter and the splitting of the lowest two levels, $2W$, using the molecular-field results, Eqs. (26)–(28). As input data we use $\epsilon = 28$ cm^{-1} = 40.3 K, $T_c = 151$ K. We include the A_2 level at

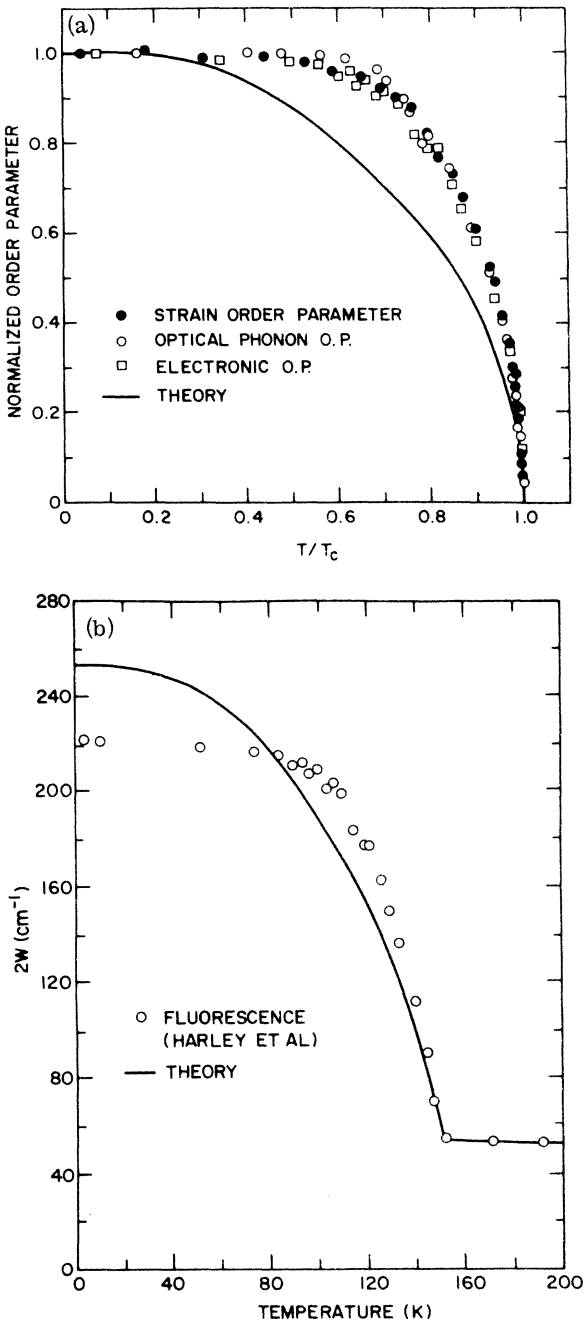

FIG. 10. (a) Normalized strain, electronic and optical-phonon order parameters vs reduced temperature below 151 K in $PrAlO_3$ (b) Fluorescence values for $2W$, the splitting of the lowest $E_g(O_h)$ doublet. The solid lines are the predictions of Ising-model-in-a-transverse-field calculations as described in the text.

~194 K explicitly by adding a term $e^{-\Delta(A_2)/T}$ to the denominator of the $\tanh(\epsilon/kT)$ factor in Eqs. (26) and (27). Equation (26) then yields immediately $J(0)+\mu = 181.5$ K. Inserting this value into Eq. (27) and (28) and solving iteratively one deduces the theoretical curves shown as the solid lines in Figs. 10(a) and 10(b). It is evident that this simple theory is in fair agreement with experiment for the splitting, $2W$, but the agreement is rather poorer for the normalized order parameter. We shall discuss the sources of this disagreement below.

As discussed in Sec. III, the twinning phenomenon below 151 K enables one to measure 2δ and thence the strain $e_{zz}-e_{xx}$ very accurately up to 0.15 K below T_c. We show in Fig. 11 a log-log plot of the twinning angle, 2δ, versus reduced temperature, $1-T/T_c$, with T_c chosen to be 150.90 K. From the figure we see that for $10^{-1} > 1-T/T_c > 10^{-3}$, the strain order parameter follows the simple power law

$$e_{zz}-e_{xx} \sim (1-T/150.9)^{0.50\pm0.02}. \tag{43}$$

Thus the critical behavior is classical in form to within 10^{-3} of the phase transition.

In general the agreement between the mean-field theory and experiment is satisfactory given the limitations of the model. The probable sources of the residual errors are (a) neglect of the higher-lying Pr^{3+} levels; (b) the Ising approximation with a constant interaction strength—both the coupling coefficient and the relevant phonon energy evolve in temperature; indeed the agreement is as good as it is for $2W$ largely because the over-all behavior is determined mainly by that near T_c, the latter in turn is correctly given by the simple theory; (c) the use of the molecular-field approximation for a Hamiltonian which is a mixture of short- and long-range interactions. It should be emphasized that the observation of a classical critical exponent, $\beta=\frac{1}{2}$, does not necessitate that the order parameter exhibit molecular-field behavior outside of the critical region. Indeed we expect all ferroquadrupolar Jahn-Teller systems to exhibit classical critical behavior since even those with predominantly short-range interactions should nevertheless have some effective long-range interaction mediated via the strains; the latter in turn should be adequate to produce classical critical behavior over the range of reduced temperature in which measurements are typically performed.

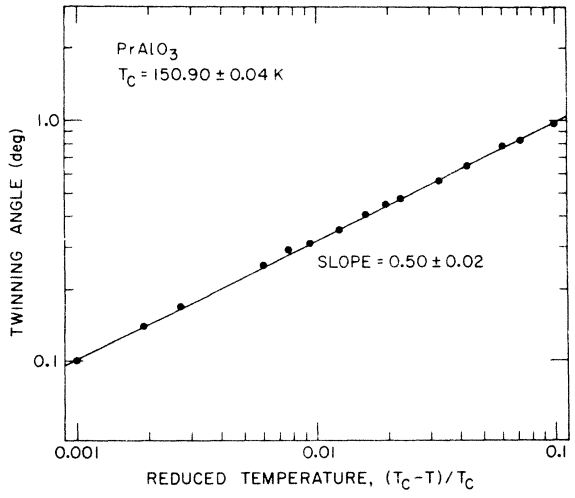

FIG. 11. Critical behavior of the twinning angle and thence the strain order parameter near T_c.

C. Dynamics above 151 K

As discussed in Sec. IV B, in the region around 151 K there should be some softening near $k=0$ of the A_1-B_1 quadrupole exciton, but the ultimate soft mode should be the $[101]_{T2}$ acoustic phonon. We now discuss measurements and analysis of these coupled quadrupole exciton–acoustic-phonon modes. From the CEF calculations presented in Sec. III, it is found that in the orthorhombic phase the A_1-B_1 magnetic dipole intensity is nearly an order of magnitude less than that of the A_1-A_2 transition; this latter excitation in turn is nearly unobservable above 151 K. Thus it is unlikely that one will be able to observe the A_1-B_1 exciton via its intrinsic neutron scattering cross section; however, it may be observable in the region of the zone where it has appreciable phonon admixture. The experiment thence reduces to a detailed study of the transverse-acoustic phonon in the [101] direction polarized along $[10\bar{1}]$. In full cubic symmetry this mode corresponds to the Σ_3 branch which has an acoustic slope determined by $\frac{1}{2}(C_{11}-C_{12})$.

In the rhombohedral phase we find the expected linear dispersion relations for wave vectors up to 0.2 reciprocal-lattice units (rlu); here $a=3.69$ Å so that $a^*=1.725$ Å^{-1} for the pseudocubic cell. Typical neutron groups at wave vectors of (0.02, 0, 0.02) and (0.14, 0, 0.14) at 210 K in the rhombohedral phase are shown in Fig. 12. These measurements were carried out with incoming neutron energies of 8.4 and 41 meV, respectively. Both spectra correspond to sharp phonon excitations with the observed profiles being fully accounted for by instrumental resolution effects. The acoustic phonon dispersion relation so-determined is shown in Figs. 13 and 14. We note that at (0.02, 0, 0.02) at 210 K there is a sharp resolution-limited peak centered about $\hbar\omega=0$. This is another example of the *central peak*[53]

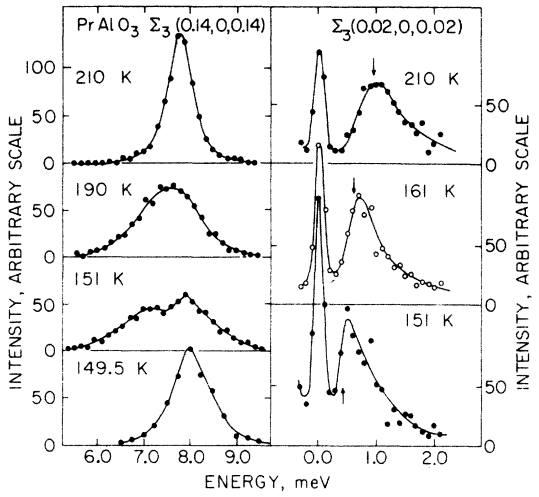

FIG. 12. Typical constant-Q scans in $PrAlO_3$ as a function of temperature. The left- and right-hand scans were carried out with incoming neutron energies of 41 (to achieve focusing) and 8.4 meV (to achieve a combination of large intensity with fine resolution), respectively. The solid lines are guides for the eye.

which has been thoroughly studied in Nb_3Sn (Ref. 54) and $SrTiO_3$.[53]

As the temperature is lowered through the first-order rhombohedral-orthorhombic transition, two distinct changes in the phonon spectra take place. Firstly, for wave vectors $< \sim 0.1$ rlu the phonon energies decrease markedly. As the temperature is decreased further toward 151 K, the softening continues while the central peak grows in intensity (see Fig. 12). The relative change in energies is most pronounced at the smallest wave vectors. We note, however, that even at the lowest wave vector accessible to us, (0.01, 0, 0.01) the acoustic phonon is both underdamped and well resolved from the central peak at $T_c = 151$ K. Thus the actual decrease of the phonon velocity to zero must be confined to wavelengths longer than those accessible to neutrons.[10] As the temperature is further decreased to 149.5 K, the phonons increase rapidly in energy towards the 210 K dispersion relation and the central peak concomitantly decreases in intensity. The phonon energies at long wavelengths as a function of temperature are shown in Fig. 13. We shall discuss the theoretical curves after first considering in more detail the question of the central peak and presenting the results at larger wave vectors.

The general features of the spectra at long wavelengths are quite similar to those near the 45-K cubic-tetragonal phase transition in Nb_3Sn. There Shirane and Axe observe a soft $[101]_{T2}$ acoustic phonon mode with an accompanying divergent central peak. In that case, they associate the central peak with the change from collision-free to collision-dominated response as the phonon frequency is lowered, and they devise a semiempirical analytic formulation for the response function which gives an excellent description of their data. The central peaks observed in $PrAlO_3$ are qualitatively similar to, albeit quantitatively different from,

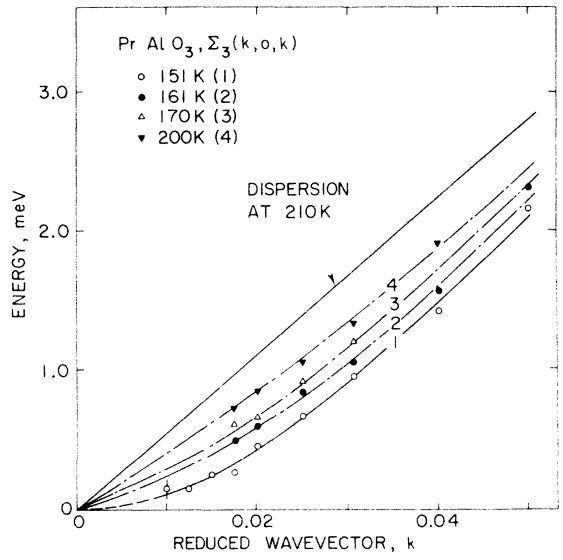

FIG. 13. $[101]_{T2}$ acoustic-phonon dispersion relation at long wavelengths as a function of temperature. The solid line at 151 K is a guide for the eye while the lines at 161, 170, 200 K are calculated using the theory of Elliott *et al.*

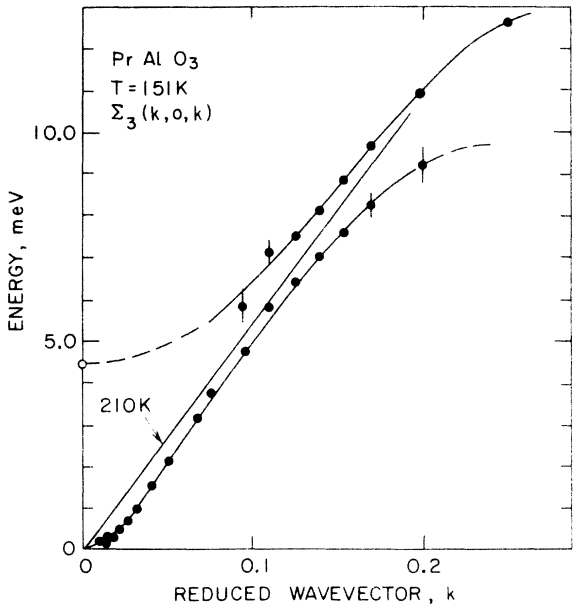

FIG. 14. Coupled quadrupole exciton–$[101]_{T2}$-acoustic-phonon dispersion relations in $PrAlO_3$. All lines are guides for the eye. The arrow at 2ϵ indicates the fluorescence value for the $A_1 - B_1$ transition energy while the open circle gives the $k = 0$ Raman value.

those observed in Nb_3Sn. In $PrAlO_3$ the temperature dependence of the peak intensity in the wave-vector regime accessible to neutrons is much less pronounced. Furthermore, strong but temperature-independent central components are observed in association with phonon branches in other directions that do not show any softening. Thus, although a consistent analysis of the $PrAlO_3$ central peak data can be made in terms of the formalism for Nb_3Sn, the results are subject to severe qualifications; in particular, the possibility that the effects originate in a mechanism of essentially a static nature cannot be excluded.

We now consider the experimental results in the region of wave vectors between 0.1 and 0.2 rlu. As discussed extensively previously and as illustrated in Fig. 9, the major effect of the rhombohedral-orthorhombic structural transition at 205 K is to lift the degeneracy of the $E(D_3)$ doublet so that the lowest two levels $A_1(C_{2v})$, $B_2(C_{2v})$ are separated by $\sim 56\ \mathrm{cm}^{-1} = 7.0$ meV in the orthorhombic phase. This value of 7.0 meV, however, is deduced from fluorescence, and hence it represents a weighted average over the whole Brillouin zone. Here we shall be concerned with the explicit A_1-B_1 dispersion relation in the [101] direction.

Typical experimental results at a wave vector of (0.14, 0, 0.14) as a function of temperature are shown in Fig. 12. When the crystal transforms from the rhombohedral to the orthorhombic phase (210 K – 190 K in Fig. 14), the phonon response shifts to lower energy and becomes much broader than the instrumental width. As the temperature is further lowered toward 151 K, a two-peaked structure clearly emerges. At 151 K, as the wave vector is increased from 0.1 to 0.2 rlu, the relative weight of the two peaks shifts rapidly from the low-frequency to the high-frequency side. The integrated intensity, however, is always just that expected on the basis of the $[101]_{T2}$ phonon response alone. This behavior is, of course, just that expected for the anticrossing of two excitations, one of which contributes essentially all of the scattering power. Two Gaussian distributions can be fitted to the observed lineshapes, and thus one is able to determine both the frequencies and the weight of the two components. The coupled dispersion relations so obtained are shown in Fig. 14. It is clear both from this figure and also from the behavior of the intensities that one is indeed observing the anticrossing of the acoustic phonon and a mode with a very small neutron scattering cross section of its own—the A_1-B_1 quadrupole exciton. Harley *et al.*[20] in their Raman data have also observed a temperature-dependent mode which has its minimum frequency around 151 K and they identify this as the $k = 0$ limit of the A_1-B_1 exciton. The energy at 151 K is shown as an open circle on Fig. 14 where it is seen to be consistent with a smooth extrapolation of our data.

It is evident that the dynamical behavior found for $PrAlO_3$ around 151 K is just that anticipated on the basis of the Elliott *et al.*[4] theory for the CJTE. We may, therefore, in turn, use the Elliott *et al.* theory to analyze the measured temperature-dependent coupled exciton-phonon excitations both to deduce the main quantities of physical interest, $J(\vec{k})$ and $K_a(\vec{k})$, and indeed as a test of the theory itself. There are two major caveats in our application of this theory. Firstly, the theory as presented in Sec. IV A is for a system with one rare-earth atom per unit cell, whereas the primitive cell of $PrAlO_3$ has two Pr^{3+} atoms related by an inversion operation. Near $k = 0$ then, the Pr^{3+} excitation will factorize into symmetric and antisymmetric modes. The Elliott *et al.* theory should, however, describe adequately the symmetric modes at long wavelengths. We thence shall use this theory directly but with the understanding that it will only be strictly valid at long wavelengths. The second caveat is that we do not have actual measurements of the A_1-B_1 exciton energy between 0.0 and 0.1 rlu. However, the dashed line shown in Fig. 14 should be an adequate interpolation between $k = 0.0$ and $k = 0.1$ and, in particular, the deduced $J(\vec{k})$, $K_a(\vec{k})$ should not be too sensitive to small deviations from this.

As discussed above, using Eqs. (33) and (34) the coupled dispersion relations at $T_c = 151$ K may be inverted to obtain $J(\vec{k}) = J_0(\vec{k}) + K_a(\vec{k}) - \mu_a$ and $K_a(\vec{k})$. As input data one uses $2\epsilon = 7.0$ meV $= 80.6$ K, $T_c = 151$ K, the 210-K acoustic-phonon slope, and the measured dispersion relations. The A_2 level at 194 K is also explicitly included in the thermal factor. For simplicity we assume that the relevant optical phonon energies are much larger than the exciton or acoustic phonon energies. This will introduce a minor quantitative error near $k = 0$. The values for the functions $J(\vec{k})$, $J_0(\vec{k}) - \mu_a$, and $K_a(\vec{k})$ so deduced are shown in Fig. 15. We see that the effective quadrupole-quadrupole interaction $J(\vec{k})$ varies rapidly with $\vec{k}$ and that at $k = 0$ the strain component accounts for about $\frac{1}{3}$ of the total interaction. The acoustic-phonon part, $K_a(\vec{k})$, is seen to be narrowly confined in k space. The effective range of the acoustic-phonon EQQI in real space is about 30 Å = 8 lattice units. This large long-range component assumedly accounts for the classical behavior observed both in the order parameter (Fig. 4) and in the specific heat.[28]

Using the deduced $J(\vec{k})$, $K_a(\vec{k})$, it is then possible to predict via Eqs. (33) and (34) the temperature dependence of the acoustic-phonon dispersion re-

lation above T_c. The theoretical curves so obtained are shown as the dashed lines in Fig. 13. It is evident that the agreement with experiment is excellent. This, we believe, represents a notable success for the theory of Elliott *et al.* Indeed this work represents the most complete test of the RPA theory to-date.

D. Dynamics of higher-lying crystal-field levels

As a final point we consider the dispersion of the higher-lying crystal-field excitons at low temperatures. For the simplest case of a single CEF level of a particular symmetry coupled to a single phonon of the same symmetry at $k=0$, the coupled dispersion relations may be written [Eq. (5.6) of Ref. 4]

$$\hbar^2[\omega^2-\omega_E^2(\vec{k})][\omega^2-\omega_p^2(\vec{k})]=4\epsilon f(T)K(\vec{k})\omega^2, \quad (44)$$

where

$$\hbar^2\omega_E^2(\vec{k})=4\epsilon^2[1-(J(\vec{k})/\epsilon)f(T)]$$

and

$$f(T)=1-e^{-2\epsilon/kT}\Big/1+\sum_{i>1}e^{-E_i/kT}.$$

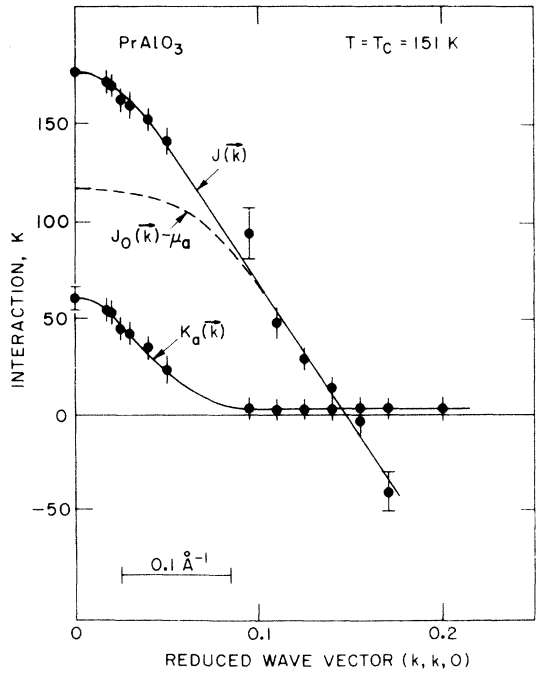

FIG. 15. Effective phonon-induced electric quadrupole-quadrupole interaction in the [101] direction in the C_{2v} phase of $PrAlO_3$. The points are deduced from the measured coupled dispersion relation shown in Fig. 13 and Fig. 14 using the RPA theory of Elliott *et al.* (Ref. 4). The contributions from the acoustic-phonon branch $K_a(\vec{k})$ and the total interaction $J(\vec{k})$ can be determined separately from the theory.

Here $K(\vec{k})$, $J(\vec{k})$ are as in Eq. (25), $\omega_p(\vec{k})$ is the bare phonon energy, the E_i's are the excited-state crystal-field energies and 2ϵ is the crystal-field splitting of the state of interest in the absence of any coupling to the phonons. In the limit of $2\epsilon \gg \hbar\omega_p \gg K(\vec{k})$, Eq. (44) simplifies to

$$\hbar\omega e(\vec{k})=2\epsilon+\left(\frac{\hbar\omega_p(\vec{k})}{2\epsilon}\right)^2K(\vec{k})f(T)+\frac{1}{N}\sum_{\vec{k}}K(\vec{k})f(T) \quad (45)$$

and

$$\hbar\omega_{p'}(\vec{k})=\hbar\omega_p(\vec{k})-\frac{\hbar\omega_p(\vec{k})}{2\epsilon}K(\vec{k})f(T).$$

Thus the phonon energy is shifted by an amount $[\hbar\omega_p(\vec{k})/2\epsilon]K(\vec{k})f(T)$ as a result of the coupling to the exciton. The exciton in turn acquires a constant shift $(1/N)\sum_{\vec{k}}K(\vec{k})f(T)$ and a dispersion given by $[\hbar\omega_p(\vec{k})/2\epsilon]^2K(\vec{k})f(T)$. The constant term $(1/N)\sum_{\vec{k}}K(\vec{k})f(T)$ just represents an additional contribution to the crystal field arising from the zero-point phonon vibrations. It will assumedly be cancelled to leading order by a similar term absorbed in ϵ in the derivation of Eq. (44) (see Ref. 4). The k-dependent term $[\hbar\omega_p(\vec{k})/2\epsilon]^2K(\vec{k})f(T)$ in Eq. (45) differs in two important respects from that in Eq. (32), the latter being appropriate to the $\omega_p \gg 2\epsilon$ regime. Firstly, the extra factor $[\hbar\omega_p(\vec{k})/2\epsilon]^2$ causes the over-all dispersion to decrease rapidly with increasing exciton energy. Secondly, the sign of this $K(\vec{k})$ term is opposite in the two equations. Thus for strongly ferroquadrupolar coupling the high-lying excitations ($2\epsilon > \omega_p$) will have maxima at $k=0$ while the low-lying excitons ($2\epsilon < \omega_p$) will have minima at $k=0$.

We now apply these results to $PrAlO_3$. In the D_{2d} phase the R_{25} phonons of the cubic phase become A_{1g} and E_g phonons with $k=0$ energies of 228 and 40 cm^{-1}, respectively.[20,38] Thus we expect on the basis of our canonical model for $PrAlO_3$ that only the E and A_1 excitons will have appreciable dispersion. This expectation is indeed confirmed by experiment. As shown in Fig. 8 and as discussed in Sec. III B, the A_1-A_2 exciton is flat to within experimental error whereas both of the A_1-E excitons have an over-all dispersion of ~1 meV. We note in addition that the A_1-E excitons have maxima at $k=0$. This in turn necessitates that the interaction is sufficiently strongly ferroquadrupolar that both $K(\vec{k})$ and $\omega_p^2(\vec{k})K(\vec{k})$ have their maxima at $k=0$. Recently, Lyons *et al.*[55] have studied the uppermost A_1 level at ~925 cm^{-1} via Raman scattering. This is a particularly attractive situation since it probably corresponds rather closely to the idealized model described by Eq. (45).

In the context of the above, a study of the crystal-field exciton dispersion relations as a function of temperature in $NdAlO_3$ would clearly be very interesting. In that case the crystal structure is rhombohedral down to 0 K with the R_{25} phonons transforming like A_1, $E(D_3)$. There should again be strong coupling of the CEF levels to these phonons. Indeed Finkman *et al.*[38] have already noted that there appear to be anomalously large electron-phonon coupling effects in $NdAlO_3$. As an aside, it is also of interest to note that a calculation of the CEF levels in rhombohedral and tetragonal $NdAlO_3$ using CEF theory identical to that we have employed in $PrAlO_3$ shows that there is very little difference in the CEF ground-state energies in the two phases. This then accounts for the fact that $NdAlO_3$ retains its rhombohedral structure down to 0 K.

Equation (45) also has some interesting consequences for the problem of energy transfer in rare earth insulators.[56-60] It has been known for some time that there may be very efficient transfer of energy over long distances in dilute crystals. This energy transfer has often been attributed to intrinsic Coulombic electric dipole-dipole interaction (EDDI). However, first-principles calculations of the EDDI seem to indicate that for parity reasons it is much too small to account for the observed transfer rates.[56,59] It is evident from our results that phonon-induced EQQ I may be orders of magnitude larger than the intrinsic multipole coupling. Thus even with the $[\hbar\omega_p(\vec{k})/2\epsilon]^2$ factor the transfer process may still be dominated by this mechanism. Calculations of the range dependence of this effective interaction have so far been concerned exclusively with overly simplified models for the phonons.[60] It is evident however, that in real systems $\omega_p^2(\vec{k})K(\vec{k})$ may have a rather complicated $\vec{k}$ dependence and, by analogy with $J(\vec{k})$ in the rare earth metals, this may imply appreciable long range components in real space. Clearly this is an important problem which deserves much more detailed investigation.

V. FUTURE EXPERIMENTS AND THEORY

We have, in this paper, presented a rather large amount of experimental and theoretical information about $PrAlO_3$. Extensive discussion and conclusions have been given in each of the subsections so we shall not repeat those here. We consider instead possible extensions of this work and the relevance to other systems. Firstly, it should now be possible to construct a comprehensive theory for $PrAlO_3$ which can account both for the 205- and 151-K transitions and which can properly predict the energies of the R_{25} phonons in the various phases. As part of this, an improvement on the Ising-model-in-a-transverse-field treatment of the 151-K transition is clearly desirable. Similarly a theoretical treatment of the high-lying exciton-phonon coupled excitations which goes beyond the simple model we have presented is of importance.

There are also a variety of experiments on $PrAlO_3$ which could both be of considerable physical interest and which should also serve to improve our understanding of this material. Of prime importance are detailed Brillouin scattering studies of the acoustic phonons around the 151-K transition. This should elucidate the full softening[10] of the $[101]_{T2}$ phonon mode at $T_c = 151$ K thereby allowing a more sensitive test of the Elliott *et al.*[4] theory. In addition, it may prove possible to measure the energy width of the *central peak* directly. $PrAlO_3$ is, in fact, especially suited for such a study in that it is one of the few transparent materials which is known to exhibit a sharp central peak near $k = 0$ above T_c. Clearly more detailed studies of the R_{25}-$B_1(C_{2v})$-phonon-$(A_1$-$B_1)$-exciton interaction are required. As shown by Harley *et al.*,[20] these two excitations exhibit complex anticrossing phenomena below $T_c = 151$ K as the exciton increases in energy and passes through the optical phonon. Indeed a proper analysis of the acoustic-phonon–optical-phonon–exciton dispersion relations below T_c as a function of temperature could prove extremely rewarding. This will undoubtedly require a much more elaborate theory than the simple heuristic treatment given here. It would also be interesting to carry out experiments as a function of hydrostatic and uniaxial pressure since this should markedly affect both the 205- and 151-K transitions. $PrAlO_3$ is also a good candidate for mixed-crystal studies, either of the form $Pr_{1-x}Nd_xAlO_3$ as already studied by Finkman *et al.*,[38] or $Pr_{1-x}La_xAlO_3$. This could give especially valuable information about the interplay between the short- and long-range interactions.

We discuss briefly the relevance of this work to other types of systems. Perhaps, the most striking feature of $PrAlO_3$ is the enormous electric quadrupole-quadrupole interactions induced by the coupling to the phonons. Indeed the phonon-induced EQQI in $PrAlO_3$ is more than a factor of 50 larger than the direct Coulombic quadrupole coupling.[33] This suggests that this enhanced EQQI may be of rather more importance in other systems than has previously been supposed. We have already discussed the implications of this for the energy transfer problem in rare-earth insulators

in Section IV D. Another class of materials where these effects could be of importance is rare earth metals and intermetallics. It has recently been discovered in the rare-earth metals that there are anomalously large k-dependent anisotropies in the ion-ion interaction.[61,62] This initially had been accredited to anisotropic Ruderman-Kittel-Kasuya-Yosida exchange. However, a significant part of this anisotropic two-ion interaction could be just the phonon-enhanced EQQI considered here. The implications of this have been discussed by Birgeneau and Kjems.[63] Recently also, Jensen[62] has shown that the anisotropies in the conal phase of erbium can be simply accounted for by including in the Hamiltonian a term of the form $\tilde{O}_2^2(J_1)\tilde{O}_2^{-2}(J_2)$—just what one expects from the EQQI.

Finally, to bring this paper full-circle, we emphasize that this work has demonstrated that $PrAlO_3$, in spite of its apparent complexity, is a prototypical example of a coupled pseudospin-phonon structural phase transition. Hopefully, the success of the physically appealing and essentially simple pseudospin approach here will encourage the continued development and application of the theory in related order-disorder problems.

ACKNOWLEDGMENTS

In the course of the present work we have profited from numerous discussions with our colleagues at Bell Laboratories and at Brookhaven National Laboratory, we have also had a number of germane conversations with those involved with the CJTE at Oxford. Among all of these we would especially like to thank John Axe, Robert Bari, Gene Blount, Elisha Cohen, Roger Elliott, Paul Fleury, Gillian and Karl Gehring, Bert Halperin, Pierre Hohenberg, Jens Jensen, Ken Lyons, Stephen Smith, and Michael Sturge.

---

*Work at Brookhaven performed under the auspices of the U. S. Atomic Energy Commission.

†On leave from AEK Risø, DK-4000-Roskilde, Denmark.

[1]As a general reference, see *Proceedings of the NATO Advanced Study Institute on Structural Phase Transitions and Soft Modes, Geilo, Norway, April 1971*, edited by E. J. Samuelsen, E. Andersen, and J. Feder (Universitetsforlaget, Oslo, Norway, 1972).

[2]Y. Yamada, Y. Noda, J. D. Axe, and G. Shirane, Phys. Rev. B 9, 4429 (1974).

[3]K. K. Kobayashi, J. Phys. Soc. Jpn. 24, 497 (1968); R. J. Elliott and A. P. Young, Ferroelectrics (to be published).

[4]R. J. Elliott, R. T. Harley, W. Hayes, and S. R. P. Smith, Proc. R. Soc. A 328, 217 (1972).

[5]J. Kanamori, J. Appl. Phys. 31, 14S (1960); 39, 688 (1968).

[6]R. Englman and B. Halperin, Phys. Rev. B 2, 75 (1970); 3, 1698 (1971).

[7]E. Pytte, Phys. Rev. B 3, 3503 (1971); 8, 3954 (1973); J. Feder and E. Pytte, *ibid.* 8, 3978 (1973).

[8]A. H. Cooke, C. J. Ellis, K. A. Gehring, M. J. M. Leask, D. M. Martin, B. M. Wanklyn, M. R. Wells, and R. L. White, Solid State Commun. 8, 689 (1970).

[9]For a review see K. A. Gehring, AIP Conf. Proc. 10, 1648 (1973).

[10]J. R. Sandercock, S. B. Palmer, R. J. Elliott, W. Hayes, S. R. P. Smith, and A. P. Young, J. Phys. C 5, 3126 (1972).

[11]S. J. Allen, Jr., Phys. Rev. 166, 530 (1968).

[12]For reviews see P. Fulde and I. Peschel, Adv. Phys. 21, 1 (1972); R. Blinc and B. Zeks, *ibid.* 21, 693 (1972); R. J. Birgeneau, AIP Conf. Proc. 10, 1664 (1973).

[13]R. J. Elliott and P. Pfeuty, J. Phys. C 4, 2370 (1971); R. J. Elliott and C. Wood, *ibid.* 4, 2359 (1971).

[14]R. B. Stinchcombe, J. Phys. C 6, 2459 (1973); 6, 2484 (1973); 6, 2507 (1973).

[15]M. A. Moore and H. C. W. L. Williams, J. Phys. C 5, 3168 (1972); 5, 3185 (1972); 5, 3222 (1972).

[16]D. L. Huber and T. Tommet, Solid State Commun. 12, 803 (1973).

[17]E. Cohen, L. A. Riseberg, W. A. Nordland, R. D. Burbank, R. C. Sherwood, and L. G. Van Uitert, Phys. Rev. 186, 476 (1969).

[18]L. A. Riseberg, E. Cohen, W. A. Nordland, and L. G. Van Uitert, Phys. Lett. A 30, 4 (1969).

[19]R. D. Burbank, J. Appl. Crystallogr. 3, 112 (1970).

[20]R. T. Harley, W. Hayes, A. M. Perry, and S. R. P. Smith, J. Phys. C 6, 2382 (1973).

[21]J. K. Kjems, G. Shirane, R. J. Birgeneau, and L. G. Van Uitert, Phys. Rev. Lett. 31, 1300 (1973).

[22]E. Cohen, M. D. Sturge, R. J. Birgeneau, E. I. Blount, L. G. Van Uitert, and J. K. Kjems, Phys. Rev. Lett. 32, 232 (1974).

[23]J. F. Scott, Phys. Rev. 183, 823 (1969).

[24]W. Cochran and A. Zia, Phys. Status Solidi 25, 273 (1968).

[25]P. A. Fleury, J. F. Scott, and J. M. Worlock, Phys. Rev. Lett. 21, 16 (1968).

[26]G. Shirane and Y. Yamada, Phys. Rev. 177, 858 (1969).

[27]J. D. Axe, G. Shirane, and K. A. Müller, Phys. Rev. 183, 820 (1969); J. K. Kjems, G. Shirane, K. A. Müller, and H. J. Scheel, Phys. Rev. B 8, 1119 (1973).

[28]E. Ryder (unpublished).

[29]J. C. Slonczewski and H. Thomas, Phys. Rev. B 1, 3599 (1970).

[30]C. Kittel, *Introduction to Solid State Physics*, 4th ed. (Wiley, New York, 1971), Chap. 4.

[31]H. Thomas and K. A. Müller, Phys. Rev. Lett. 21, 1256 (1968).

[32]J. Feder and E. Pytte, Phys. Rev. B 1, 4803 (1970).

[33]W. P. Wolf and R. J. Birgeneau, Phys. Rev. 166, 376 (1968).

[34]R. A. Cowley, Phys. Rev. 134, A981 (1964).

[35]See R. Englman, *The Jahn-Teller Effect in Molecules and Crystals* (Wiley, New York, 1972); M. D. Sturge, Solid State Phys. 20, 91 (1967).
[36]T. Riste and K. Otnes, Nucl. Instrum. Methods 75, 197 (1969); G. Shirane and V. J. Minkiewicz, *ibid.* 89, 104 (1970).
[37]H. Unoki and T. Sakudo, J. Phys. Soc. Jpn. 23, 546 (1967).
[38]E. Finkman, E. Cohen, and L. G. Van Uitert, in *Proceedings of the Second International Conference on Light Scattering in Solids*, edited by M. Balkanski (Flammerion, Paris, 1971) p. 369; Phys. Rev. B 7, 2899 (1973).
[39]See for example, K. C. Turberfield, L. Passell, R. J. Birgeneau, and E. Bucher, Phys. Rev. Lett. 25, 752 (1970); J. Appl. Phys. 42, 1746 (1971).
[40]W. Marshall and S. W. Lovesey, *Theory of Thermal Neutron Scattering* (Clarendon, Oxford, England, 1971), p. 169. See also R. J. Birgeneau, J. Phys. Chem Solids 33, 59 (1972).
[41]A. Kiel and S. P. S. Porto, J. Mol. Spectrosc. 32, 458 (1969).
[42]G. H. Dieke, *Spectra and Energy Levels of Rare Earth Ions in Crystals* (Wiley, New York, 1968).
[43]For a discussion of the theory, see M. M. Ellis and D. J. Newman, J. Chem. Phys. 49, 4937 (1968), and references contained therein.
[44]H. A. Buckmaster, Can. J. Phys. 40, 1670 (1962); D. Smith and J. H. M. Thornley, Proc. Phys. Soc. Lond. 89, 779 (1966).
[45]R. J. Birgeneau, Can. J. Phys. 45, 3761 (1967).
[46]R. J. Elliott and K. W. H. Stevens, Proc. R. Soc. A 218, 553 (1953).
[47]M. T. Hutchings, Solid State Phys. 16, 227 (1964).
[48]R. Sternheimer, M. Blume, and R. F. Peierls, Phys. Rev. 173, 376 (1968).
[49]M. T. Hutchings and D. K. Ray, Proc. Phys. Soc. Lond. 81, 663 (1963).
[50]M. I. Bradbury and D. J. Newman, Chem. Phys. Lett. 1, 44 (1967).
[51]E. I. Blount, Ref. 22, 55 and private communication.
[52]M. Born and K. Huang, *Dynamical Theory of Crystal Lattices* (Clarendon, Oxford, England, 1954).
[53]T. Riste, E. J. Samuelsen, K. Otnes, and J. Feder, Solid State Commun. 9, 1455 (1971); S. M. Shapiro, J. D. Axe, G. Shirane, and T. Riste, Phys. Rev. B 6, 4332 (1972).
[54]J. D. Axe and G. Shirane, Phys. Rev. B 8, 1965 (1973).
[55]K. B. Lyons, R. J. Birgeneau, E. I. Blount, and L. G. Van Uitert (unpublished).
[56]R. J. Birgeneau, Appl. Phys. Lett. 13, 193 (1968); J. Chem. Phys. 50, 4282 (1969).
[57]See, for example, L. G. Van Uitert, J. Electrochem. Soc. 114, 1048 (1967).
[58]D. L. Dexter, J. Chem Phys. 21, 836 (1953); Phys. Rev. 126, 1962 (1962).
[59]J. D. Axe and D. F. Weller, J. Chem. Phys. 40, 3066 (1964).
[60]R. Orbach and M. Tachiki, Phys. Rev. 158, 524 (1967).
[61]R. M. Nicklow, N. Wakabayashi, M. K. Wilkinson, and R. E. Reed, Phys. Rev. Lett. 27, 334 (1971).
[62]J. Jensen, Riso Report No. 252 (unpublished). A. E. K. Riso (Roskilde, Denmark, 1971) (unpublished).
[63]R. J. Birgeneau and J. K. Kjems, AIP Conf. Proc. 18, 1066 (1973).